

¹ Masters Thesis: The Evolution of Fault Slip
² Surfaces with Cumulative Displacement

³ Kelian Dascher-Cousineau

⁴ May 7, 2017

⁵ **Abstract**

⁶ Fault slip surface roughness determines fault strength, friction and dy-
⁷ namic fault processes. Wear models and field observations suggest that
⁸ roughness decreases with cumulative displacement. However, measurements
⁹ have yet to isolate the effect of displacement from other possible controls,
¹⁰ such as lithology or tectonic setting. We present an unprecedentedly large
¹¹ fault surface dataset collected in and around the San-Rafael Desert, S.E.
¹² Utah, United States. In the study area, faults accommodated regional ex-
¹³ tension at shallow 1 to 3 *km* depth and are hosted in the massive, well
¹⁴ sorted, high porosity Navajo and Entrada sandstones. Existing detailed
¹⁵ stratigraphic throw profile provide a maximum constraint for displacement.
¹⁶ Where cross-sectional exposure is good, we measure exact displacement im-
¹⁷ parted on slip surfaces using offset in marker horizons. Thereby, we isolate
¹⁸ for the effect of displacement during the embryonic stages of faulting (0
¹⁹ to 60 *m* in displacement). Our field observations indicate a clear compo-
²⁰ sitional and morphological progression from isolated joints or deformation

bands towards smooth, continuous and mirror-like fault slip surfaces with increasing displacement. To quantify these observations, slip surfaces were scanned with a white light interferometer, a laser scanner and a ground based Lidar. Together these instruments resolve more than eight decades of spatial bandwidth (from less than μm 's to m 's in scale). In so doing, to the best of our knowledge, we increase the existing data on published fault topographies by XXX fold (available HERE). Results indicate that roughness as defined by the power (P) at a given wavelength (λ) decreases with displacement (D) according to a power law, $P(\lambda) \propto D^{0.6 \pm 0.1}$. Trends are however subject to significant scatter. Roughness measurement associated with only maximum constraints on displacements corroborate this result—for a given displacement, minimum roughness is bounded by the later smoothing trend. In addition, we find that the maximum roughness is fixed—bounded a by a primordial roughness corresponding to that of joints surfaces and deformation band edges. Building upon our results, we propose a wear model to explain the evolution of faults with displacement. The basis of the model is supported by numerical simulations of crack initiation and growth using boundary element models Fri2D and growth by work-minimization (GROW). Our modelling provides the first insight into fault slip surface process consistent with observational constraints, i.e. fractal geometry and a nearly power-law decay with displacement, by using calling upon scale dependent strength, strength heterogeneity and scale invariant asperity failure by truncation.

⁴⁴ **Contribution of Authors**

⁴⁵ **1 Introduction**

⁴⁶ **1.1 Context**

⁴⁷ Faults are a characteristic feature of the Earth’s brittle crust. Crustal permeability,
⁴⁸ seismicity and mineralization are just few systems upon which faults act as major
⁴⁹ controls [79] [80]. In spite of their importance, some aspects of faults and their
⁵⁰ underlying processes remain poorly understood. What are the frictional proper-
⁵¹ ties of faults? How strong is a fault? How do faults mature? Key factors such as
⁵² pore pressure [16], mineral composition [82] and fault architecture [24] [25] have
⁵³ been shown to have important roles in answering these questions. However, these
⁵⁴ factors often fail to explain the highly heterogeneous, chaotic and hierarchical be-
⁵⁵ haviour of faults. Complex fault geometry has long been proposed as a key factor
⁵⁶ in the faulting process. However, a detailed and robust exploration of the impli-
⁵⁷ cations thereof has only recently garnered increasing attentions. This change of
⁵⁸ pace mainly owes to advances in the mathematical theory behind complex natural
⁵⁹ systems [51] [50], the rapid increase computational power, technological advances
⁶⁰ in high resolution surveying tools (GPS, photogrammetry and Lidar) and detailed
⁶¹ field studies of fault architecture [73] [21]. Fault geometry has since been included
⁶² as a key component of wholistic explanations for the mechanical behavior and
⁶³ evolution of faults (e.g. [46] [1] [73]).

⁶⁴ Fault zones generally comprise of a damage zone and fault core – whereby the
⁶⁵ damage zone represents the halo of subsidiary fault features including smaller
⁶⁶ fault, fractures, cleavage and veins; the faults core generally represent zone in

which most of the displacement has taken place and is associated with intense comminuitons of the protoloth [79] [24] [17]. Actual Slip on a fault occurs on discrete slip surfaces within the fault core [58] [35] [5]. These surfaces are not planar; they are rough [22]. Slickenlines, corrugations, mullions and jogs are all fault slip surface features which reflect the multiscale nature of fault roughness [73] [65]. Field studies have found common characteristics in the statistical properties which describe the topography of fault surfaces. These can be summarized as follows: 1) Fault surfaces topographies appear to be well defined by large fractal domains, wherein 2) faults are smoother at larger length scales [73] [22] and 3) are rougher in the slip perpendicular direction than in the slip parallel direction [47].

Fault roughness has been demonstrated to be critical in determining fault properties and corresponding scaling relationships. A series of field investigations, laboratory experiments, analytical predictions and numerical simulation have explored the heterogeneous stresses and deformation patterns around complex fault geometries around single fault steps, ramps and jogs (e.g. [7], [75], [53], [43], [15]), on simple theoretical fault geometries (e.g. [27]; [26]), and real or synthetic faults with geometrically fractal bandwidths in two dimensions (e.g. [67], [39], [34], [63] and three dimensions (e.g. [56]; [?], [77], [87]; [86]). Direct repercussion of complex stress patterns include the following: increased geometrical shear resistance or "roughness drag" [36]; increased and spatially variable off-fault damage and fracture energy [57] [26] [39]; reduced stress drop [87] and impeded slip budget [33]. In numerical simulations, Zielke et al., 2017, reports a nearly two-fold decrease in earthquake moment release for a fault with realistic roughness compared to its planar counterpart. Laboratory experiments comparing smooth and rough surface show that with increasing roughness, friction increases [8], slip stability decreases,

92 critical slip distance increases and rupture nucleation dimension increases with
93 surface roughness [?] [40]. These features do appear in earthquake statistics. Bol-
94 stered by numerical simulations of complex stress fields, Parsons, 2008, found that
95 persistent clusters and gaps in seismicity can be attributed to geometrical com-
96 plexities on faults.

97 It is increasingly evident that roughness is both a fingerprint of the funda-
98 mental features of- and an active agent in the faulting process [73] [13] [20]. In
99 accordance, incorporating more complex sources geometries has become a more
100 frequent practice in dynamic earthquake rupture modelling and slip inversions
101 (e.g. [77], [55], [87].

102 The magnitude in roughness is highly variable. While there has been significant
103 progress in understanding the active role of roughness in the faulting process, it
104 remains unclear what determines the complexity of fault geometry (e.g. [21], [13]).
105 Sagy et al. (2007) noted a systematic decrease in roughness of ‘mature’, large
106 displacement faults compared to ‘immature’ faults with low displacements. Similar
107 results have been observed along reactivated joints, in laboratory experiments [32],
108 and in compilations of fault roughness analysis [12] [19]. However, these data
109 show only weak correlations between fault roughness and cumulative displacement
110 [12] [21]. These results are also put in question by later experiments showing
111 roughening with shear with normal loads higher than 7.5 MPa [6].

112 Relating fault roughness to cumulative displacement is not trivial. Experi-
113 ments cannot perform tests with realistic roughness over large enough displace-
114 ment. It is also unclear how laboratory experiments scale up to natural faults.
115 Exhumed fault slip surfaces are rarely well preserved. Furthermore, obtaining
116 well-constrained displacement estimates is contingent on the presence of precise

and accurate kinematic indicators (e.g. piercing points). Additionally, combining observations over a broad range of displacements is challenging. Consequently, it is unclear whether trends observed in compilations of roughness measurements from multiple faults are directly attributable to displacement or a combination other geological factors. For instance, while comparing fault surfaces from geologically diverse datasets, variations in lithology, faulting regimes, temperature and depth may all be introducing further systematic variations.

The existence of a distinction between mature and immature faults and the precise characterization of this transition has far-reaching implications. As discussed above, earthquake sources parameters are sensitive to fault roughness. Correspondingly, an evolution of roughness with displacement implies that "not all fault should be treated equally". This prediction is consistent with more efficient energy radiation measured on mature faults compared to immature faults [41]; and changes in b-values associated to fault off-set [81]. Additionally, the evolution of roughness represents a novel insight into the architecture of a fault zone. The geometry of the fault surface modulates the architecture of the whole fault zone [39] [63]. Changes in roughness require interaction between the slip surfaces and its direct surrounding (fault core), resulting in the formation of fault rock [60] and off-fault damage [39] [63]. The co-evolution evolution of the fault slip surface and the fault zone as a whole is a novel insight the maturity of fault from a structural point of view.

₁₃₈ **1.2 Fault Roughness**

₁₃₉ The deviation of fault surfaces from planarity formally defines roughness [14].
₁₄₀ Pioneering studies used contact profilometers to measure the roughness of fracture
₁₄₁ and fault surfaces along discrete profiles [51] [14] [73] [61] [59]. Combined with
₁₄₂ the surface profile of the San Andreas fault, faults were found to exhibit fractal
₁₄₃ scaling over a remarkably broad range of length scales ranging over 10 orders of
₁₄₄ magnitude—from 10^{-5} to $10^5 m$ [73] [61] [3]. Over these length scales, fractal
₁₄₅ scaling is said to be statistically self-affine [51] [50].

₁₄₆ A statistically self-affine profile along x with heights $h(x)$, is invariant under
₁₄₇ the affine transformation:

$$\begin{cases} x \rightarrow \lambda x \\ h \rightarrow \mu h \end{cases} \quad (1)$$

₁₄₈ This relation therefore implies an exponential relation between the scaling, λ
₁₄₉ (along x), and μ (along h) such that:

$$\mu = \lambda^\varsigma \quad (2)$$

₁₅₀ Where ς is a constant named the Hurst exponent [69].

₁₅₁ Many analytical methods exist to quantify the fractal roughness of faults [50]
₁₅₂ [71] [19]. Possibly most intuitive of which is the Root Mean Squared (*RMS*) as a
₁₅₃ function of scale. It is effectively a measure of topographic variance. For a given
₁₅₄ profile of length L with a point spacing of Δx with deviation h from the best fit
₁₅₅ line, the *RMS* is defined as follows:

$$RMS(L) = \sqrt{\frac{\Delta x}{L} \sum_{i=1}^{L/\Delta x} h_i^2} \quad (3)$$

156 The *RMS* roughness of a fault or fracture exhibits power-law scaling with seg-
 157 ment length. A self-affine profile should therefore plot as a straight line on a log-log
 158 plot of the *RMS* as a function of the segment length with a slope equivalent to
 159 the Hurst exponent [71]. The most conventional approach to describe the fractal
 160 roughness of faults has instead been the power spectrum and variations thereof
 161 (i.e. amplitude spectrum and power spectral density). By testing various frac-
 162 tal analytical tools on synthetic profiles [71] and surfaces [19], the power spectral
 163 analysis was shown to yield estimated of scaling exponent most robust to system
 164 size and Hurst exponent values. For a set of discretely sampled points, the power
 165 spectrum of a profile is the result of a Fourier transform. In practice it is obtained
 166 using a Fast Fourier Transform algorithm (FFT). The power spectrum defines a
 167 two dimensional surface profile as linear superposition of sinusoidal profiles dis-
 168cretized over a fixed frequency domain. In the frequency domain, rougher profiles
 169 will have correspondingly higher amplitudes, or power. The power spectrum of a
 170 self-affine profile defines a power-law:

$$P(k) = Ck^{(-1-2\zeta)} \quad (4)$$

171 Where $P(k)$ is the power at a given spatial frequency, k , C is the pre-factor and
 172 ζ is the Hurst exponent [50] [59] [69] [21].

173 Pioneering studies suggested that fault surfaces were approximately self-similar.
 174 Self-similarity represents a self-affinity with a Hurst exponent is 1 [50]. The devel-
 175 opments in laser scanner technology over the past decade, particularly terrestrial

laser scanners, enabled the detailed characterization of slip surfaces in three dimension [47] [44] [66] [65] [42] [9] [12] [21]. Later studies averaging result cross sectional profiles through a fault surface suggested that smaller Hurst exponent may better characterize fracture surfaces and faults (e.g. [47] [69] [65] [20] [21]). Studies of natural mode I crack surfaces have observed radially sym self-affinity with a Hurst exponent of ~ 0.8 at all scales of observation ([70] [10]-and references therein). Shear, or mode II cracks (i.e. faults) were found to differ in that they are anisotropic. The Hurst exponent parallel to shear (~ 0.6) is smaller than that in the shear-perpendicular direction (~ 0.8) [47] [66] [9] [21]. Overall, observations also show that fault surfaces have distinctly smoother profiles along slip direction than perpendicular to slip [47] [?] [21]. The magnitude of the roughness in both directions is, however, subject to a substantial spread in values over many orders of magnitude [21] [12]. This variability is most strongly reflected in the pre-factor. Recent studies also report a minimum length scale of grooving, a length scale at which slip surface is no longer anisotropic [18] [13]. This transitions typically occurs around 4 to 500 μm and roughly corresponds to where the fractal scaling in the slip parallel and slip perpendicular direction meet.

Why are slip surfaces fractal? The fractal character of slip surfaces can be explained by a range of processes. There is, however, no clear consensus in the existing literature. Candidate explanations include the superposition of random wear processes processes, random fracture tip growth, and more ... Perhaps most topical is the proposition of scale dependent strength as proposed by Brodsky et al., 2016. Using the aspect ratios of geometrical asperities as a measure of rock strength at a given scale, it is argued that fractal character of fault surfaces directly reflects a scale dependence in rock strength. Moreover, a break in fractal scaling at

201 the $\approx XXX\mu m$ length scale is interpreted as a transitions from inelastic or brittle
202 processes (large scales) to plastic processes. This explanations is in agreement with
203 laboratory experiments that report that larger volumes of rock are, on average,
204 weaker ...

205 Fractal characterizations of surfaces do not uniquely define a profile or surface.
206 Other statistical metrics exist and are common place in many engineering practices.
207 Specifically, examining the statistical distribution of the height measurements of
208 a surface provides insight into the contact [?], frictional behavior [?] and wear
209 processes [2].

210 define skewness, kurtosis, etc.

211 The the statistical moment is defined as follows:

212 First ($m = 1$) and second ($m = 2$) order

213 **1.3 The evolution of slip surfaces with displacement**

214 *this could be in an interpretation section

215 Previous work has mainly associated fault surface deformation to mechani-
216 cal wear processes as the dominant mechanism of surface evolution [60] [66] [12].
217 Mechanical wear processes include any erosive process in which volume removal
218 is frictionally induced from surfaces in sliding contact. Before further exploring
219 the effects of wear in fault slip surfaces, it is worth recognizing that many other
220 processes could—and likely do—cause the slip surface to evolve with displacement.

221 A surface can change according to the following:

222 *surface deformation*

223 *Addition of material*

224 *Removal of material*

225 Fault slip surfaces have evidence pointing to each of these processes preserved
226 in the rock record.

227 *Surface deformation* encompasses any process by which a surface changes shape
228 by the rearrangement of material (no removal or addition). Both elastic and
229 inelastic processes allow fault blocks to deform. At the seismic time-scales, only
230 elastic and brittle deformation can occur—whereby macroscopic fault damage and
231 micro-fractures in grains and crystals away from the fault can enable stain and
232 dissipate stress on the fault. At longer time-scales, calcite twinning, pressure
233 solution, and clay alteration can also occur yield similar effects. These short and
234 long-time scale mechanisms define the visco-elastic rheology of fault blocks.

235 It is unlikely that the rheology of the fault block and its effect on the slip
236 surface topography are significant in the evolution of the slip surface. Using slick-
237 enline orientations and fault core thickness as a proxy to the fault block rheology
238 Kirkpatrick et al. 2014, find that 1) deformation does occurs in fault block and 2)
239 there is a scale dependence to this deformation whereby. However, this scaling is
240 not well represented in fault geometric scaling. It would rather predict a change in
241 scaling at the outcrop scale. The absence of any such signal in the topography of
242 fault slip surfaces implies that deformational processes cannot directly determine
243 how slip surfaces evolve with displacement.

244 For its part, an *addition of material* occurs as fault rock is cemented onto slip
245 surfaces—filling in geometrical concavities and effectively reducing the amplitude
246 of surface irregularities. Its effect is preserved in the rock record with mobile, or
247 *fluidized*, gouge cemented and re-fractured in subsequent faulting [65] [76]. More-

248 over, it has been shown that discrete slip surface can arise from the localization of
249 shear strain within unconsolidated granular material (e.g. [23]). It is key to note
250 that this, and similar, mechanisms are then metered by the healing-rate and the
251 wear-rate.

252 *removal of material* is caused by mechanical wear. As fault blocks slide past
253 each other, frictional wear is an inevitable process. Layers of comminuted fault
254 rock, cemented or not, are direct evidence of this process [60] [74]. Wear is known
255 to be multiscale. At small scales, grains can be plucked or broken [76]; at larger
256 scales grains plough slip surfaces to create corrugations [72] and sidewall ripouts
257 form [83]. It is key to note that 1) all these processes fall under the definition
258 of wear in that they involve the failure of geometrical protrusions, only these are
259 expressed at various scales and 2) these have substantive impact on the surface
260 geometry.

261 MAKE FIGURE HERE FOR REFERENCE SIMILAR TO THE ONE IN
262 YOUR EPSL SLICKENLINE/RHEOLOGY PAPER - but focus on the fact that
263 there is an ty failing.

264 While wear processes are subject of a vast field of research, particularly in
265 engineering and tribology due to interest in manufacturing machine parts for
266 longevity [54], its applications in the earth sciences is emergent with tests mainly
267 conducted at laboratory scales [60] [74] [84] [?]. The only applications to natural
268 fault surfaces is a prediction of wear volume presented in Brodsky et al., 2011.

269 The wear rate, the volume of wear-product produced per unit offset is broadly
270 related to the real area of contact and loading. When two surfaces are put in
271 direct contact, the real area of contact is much smaller than the nominal surface
272 areas because the load is supported at microscopic protrusions from a surface, or

273 *asperities* ([2], [38] [11], [?]). Remote loading normal to the surface causes local
274 stresses and associated deformation at contact points. Note that as the load is
275 increased, deformation of large asperities causes new asperities to come in contact.

276 In its simplest form, wear rate ($\frac{\partial V}{\partial x}$) defined to be proportional to the remote load
277 (P):

$$\frac{\partial V}{\partial x} \propto P \quad (5)$$

278 The relation has been shown to be reasonably robust in experimentation for
279 most materials. In further detail, the size, distribution and duration of contact
280 areas, as well as the shape of the worn particles, control the general behaviour of
281 wear. Note that material properties are contained in a constant of proportionality
282 referred to as the probability factor—the probability of a collision of asperities to
283 lead to removal of material [2].

284 Following this formulation, Scholz, 1987, proposed that wear rate for faults
285 could be determined as a linear relationship with displacement and an inverse rela-
286 tionship with hardness. The displacement relationship is in reasonable agreement
287 with laboratory experiments [85] and measurements of natural fault rock thick-
288 ness [64] [78]. The hardness dependence is difficult to test given uncertainties in
289 both fault rock thickness and hardness [74]. The simple formulations forwarded
290 by Archard, 1953, and its application to faults by Scholz, 1987, was acknowledged
291 to have serious limitations in their applications to natural faults. Specifically, the
292 author raises concerns about the surface geometry of real fault, and about the
293 scaling and effectiveness of wear processes such as grains plucking and fault rock
294 abrasion.

Building off of experiments on engineering metals [62] and ceramics [48], new fault wear model integrated a 'running-in' component which exponentially decays towards steady-state [60] [84]. This behavior intruced a discrete such that the volume of fault rock produced (V) can be expressed as a function of displacement (x) according to:

$$V = \beta [1 - \exp(-nx)] + Kx \quad (6)$$

Where β , n , and K are constants.

A running-in stage is though to reflect effect of surface roughness. This later formulations was supported by a semi-analytical formulations of asperity failure and rotary shear experiments. However, in line with comments in Power et al., 1988, we propose that this running-in stage on real faults is likely to be substantially different for faults where fractal topography implies that new larger asperities will come into contact with increasing displacement. Laboratory experiments have limited fractal bandwidth. Shear boxes are limited to sample length; rotary shear apparatus are limited to their circumference length. We highlight that wear processes controlling the behaviour laboratory scale experiments are likely inadequate for natural faults. These may instead reflect relict behaviour issuing from limited fractal bandwidth and emplacement of mobile gouge layers buffering the surfaces.

It is clear that the fractal nature of fault surfaces is important to reconcile with a model of wear. However, concepts of fractal scaling, strength heterogeneity and scale dependent strength are poorly captured by the current literature. Moreover, notwithstanding controversial fault rock-displacement scaling relationship, existing models hold nearly no basis in field observations of wear processes and fault surface

317 geometry. If wear is to represent the mechanism that defines slip surface geometry,
318 a common thread must exist between scales (processes outlined in figure XXX) for
319 slip surfaces to remain fractal with increasing displacement.

320 **1.4 Objectives**

321 This study seeks to fill a fundamental knowledge gap in the field of structural geol-
322 ogy and earthquake mechanics. While it is increasing evident that fault roughness
323 is an important agent in the earthquake process, it is still unclear what defines
324 the magnitude and large spread in roughness of fault slip surfaces. To do so we
325 test the two following hypotheses: 1) fault slip surface geometry is defined by its
326 displacement history wherein 2) wear is the dominant mechanism of slip surface
327 evolution.

328 These hypotheses are tested according to three lines of inquiry:

329 1. investigation of fault architecture and microstructure of faults in the San
330 Rafael Desert, Utah (section ??). Observations have a specific focus on
331 recording qualitative changes from zero displacements structures such as de-
332 formations bands and joints, to small displacement faults (centimeters of
333 displacements) and finally to larger faults (meters of displacement). We also
334 pay careful attention to the mechanisms that alter the slip surface geometry.

335 2. geometric analysis of pristine fault surfaces preserved in the San Rafael
336 Desert , Utah, using scan data aquired in the field using a Lidar and a
337 laser scanner, and in the laboratory using white light interferometry (section
338 ??).

339 3. numerical modelling failure of asperities using Boundary Element Modelling
340 (BEM) applied to frictional faults in two dimension (Fric2D - [30] [29] [28]
341 [68]) and crack growth by work-minimizations (GROW - [52]) (section ??).

342 Building upon the results from each component, we propose a wear model for
343 fault surfaces. This model calls upon scale dependent strength, strength hetero-
344 geneity and scale invariant asperity failure processes (section ??). Note that links
345 the scans of fault slip surfaces, Matlab scripts to process and analyse slip surfaces
346 and detailed documentation is available in the appendix.

347 2 Tectonic Setting

348 This study takes advantage of exceptionally well exposed faults in the San Rafael
349 desert of south-central Utah. The San Rafael Desert hosts a sequence of gently
350 dipping marine and sub-areal sedimentary rocks deposited from the Pennsylvanian
351 to the Jurassic (see Figure 2). The San Rafael Desert is part of the San Rafael
352 Swell, a monocline that formed when these sediments were uplifted as a passive
353 drape fold above a reactivated basement reverse fault during the Late Cretaceous
354 Laramide Orogeny (Kelly, 1955; Vrolijk et al., 2005). In turn, the swell is part of
355 the broader Colorado Plateau (Kelly, 1955). Networks of joints and normal faults
356 caused by Laramide activity cross-cut the sedimentary sequence and accommodate
357 North-South extension (Aydin and Johnson, 1978; Vrolijk et al., 2005). Within the
358 San Rafael Swell we focus the following field locations: 1) the Chimney Rock Fault
359 Array (Navajo Sandstone), 2) the Big Hole fault (Navajo Sandstone), 3) faults
360 outcropped in the Iron Wash (Navajo Sandstone) and 4) a network of deformation
361 bands near Goblin Valley State Park (Entrada Sandstone) (see figure XXX).

362 Advantages of these field locations are manifold. First, the nearly pure quartzite
363 lithology, extensional tectonic regime, depth (2-4 km or 40-80 MPa), temperature
364 (estimates range from 45-90 °C) of activity, and faulting mechanism are all rela-
365 tively consistent (Vrolijk et al., 2005). Consistency in these parameters is key to
366 isolating the effect of displacement on the fault roughness. Moreover, both field
367 locations exhibit well preserved fault surfaces that are exposed and accessible (see
368 Figure 3).

369 The Chimney Rock fault array is an orthorhombic set of faults that crops out
370 at the northern end of the San Rafael Swell ([45], Davatzes et al., 2003). Two
371 pairs of oppositely dipping normal faults crop out at the surface with preserved
372 fault scarps. WNW-striking faults are interpreted to have formed by shear reac-
373 tivation of joints, whereas ENE-striking faults initially formed from deformation
374 bands (Davatzes, 2003). Exposure is very good, faults are abundant and have well
375 preserved fault surfaces (Vrolijk et al., 2005). The Chimney fault array has stud-
376 ied to better understand of fault geometry (Shipton and Cowie, 2001; Shipton and
377 Cowie, 2003), permeability (Shipton et al., 2002) and kinematics ([45]; [45]; [49];
378 Davatzes et al., 2003) . As a result, detailed maps of the fault array have been pro-
379 duced (e.g. [49]) . In addition, by using measurements of the separation between
380 footwall and hanging wall cutoffs of sedimentary horizons, entire displacement pro-
381 files have been measured for faults with a wide range of displacements (Cowie and
382 Shipton, 1998; [49]; Shipton and Cowie 2001; Shipton and Cowie, 2003). The Big
383 Hole fault is located just to the South-East of the Chimney Rock Fault Array.
384 While not explicitly part of the fault array, the Big Hole fault shares a nearly
385 identical geological setting. The Big Hole fault has been extensively studied in
386 detail as an analog to hydrocarbon reservoir-scale faults. Displacements on the

387 exposed fault range from 8 m to 39 m. (Shipton and Cowie, 2001; Shipton and
388 Cowie, 2003) Large networks of deformation band faults outcrop near Goblin Val-
389 ley State Park on the southeastern margin of the San-Rafael Swell (Aydin and
390 Johnson, 1978). Deformation bands are the result of concentrated shear deforma-
391 tion on narrow centimeter thick bands (Aydin and Johnson, 1978; Davatzes et al.,
392 2003). Collapsing pore space, and grain crushing accommodates this deformation.
393 Deformation bands are interpreted as the embryonic stages of fault development
394 (Fossen and Hesthammer, 1998; Fossen et al., 2007). Because deformation bands
395 dramatically alter the local permeability structure, Goblin Valley has been exten-
396 sively studied in light of fault nucleation and the implications for hydrocarbon
397 circulation (e.g. Fossen et al., 2005; Tobari and Fossen 2009). At Goblin valley,
398 arrays of deformation bands anastomose—outcropping as centimeter- to meter-
399 sized slabs. These are often bounded by discrete slip surfaces with well-preserved
400 striations — i.e. roughness (Aydin and Johnson, 1978). Offsets in sedimentary
401 beds have allowed previous studies to obtain detailed displacement measurements
402 (e.g. Schultz and Fossen 2002). Together, these field locations offer the chance to
403 survey well-preserved fault surfaces that have hosted displacements from embry-
404 onic stages to 30 m of displacement. Moreover, novel to this study, we are able to
405 survey multiple expressions of a single fault’s surface with various displacements
406 according the displacement profile of the fault.

407 2.1 Faulting in Sandstone

408 Faults in well sorted Sandstones provide a natural laboratory for the study of fault
409 maturation and have correspondingly been subject of extensive study (e.g. A LOT

⁴¹⁰ OF CITATIONS). Its is however important to recognize

Loca- tion	Lithology	Description	Displacement Constraints
Chim- ney Rock Fault Array	At the contact between the Navajo Sandstone and the base of the Carmel Unit	Orthorombic set of normal faults with preserved faults scarps of Navajo Sandstone	Displacement profiled of stratigraphic throw constrained by offset on a Carmel Limestone Marker Horizon by Maerten et al., 2000.
21	Big Hole Fault	One single large normal fault structure partitioning displacement on two major strands traceable for kilometers through a river wash with scarp exposure, and strike parallel/perpendicular cross-sectional exposure	Displacement constrained using the top Erosionally competent horizon at the top of the Navajo by Shipton and Cowie, 2003 and directly where possible.
411	Iron Wash	Network of normal and strike-slip cross-cutting faults. Little scarp exposure but has good cross-sectional exposure with fresh slip surfaces (using hammer and chisle)	Displacement mostly constrained by direct measurement of offset in the Upper Navajo horizon.
Molly's Castle	Entrada Sandstone	East-West striking network of normal faults and ubiquitous deformation bands. Well preserved slip surfaces broadly	Displacement constraints available in places from mapping by Aydin (1978) and directly measured using various marker

412

Table 1: Table caption

22

413 3 Field observations and Microstructure

414 We report on the fault architecture in the Navajo and Entrada Sandstones with
415 a specific focus on the evolution from zero-displacement structures such as joints
416 and deformation bands to large offset structures with polished slip surfaces and
417 accompanying fault rock lithologies.

418 3.0.1 Zero-Displacement Structures

419 Deformations bands and joints are a ubiquitous and characteristic feature around
420 faults in high porosity sandstones [37] [31]. Larger fault structures nucleated from
421 pre-existing networks of deformation bands and joints [31]. Deformation local-
422 izes and intensifies in and along theses structures and eventually form through-
423 going faults [4]. The characteristics and surface morphology of the local zero-
424 displacement features are especially relevant to our analysis as they represent the
425 original, zero displacement, roughness of faults in in the study area. This in is
426 fundamental to understanding the integrated maturation path of slip surfaces to
427 larger displacements

428 In outcrop, deformation bands, also known as shear bands are sinuous white
429 lineaments, 1 to 5 millimeters in thickness, that accommodate small strain typi-
430 cally as shear shear offset. Shear bands are a unique feature to coarse, well sorted
431 sandstones. In sandstones, small strains can be accommodated by the localization
432 of run-away collapse of grains in sub planar sheets [37]. In thinsection, bands
433 are associated with a gradational reduction in grains size towards their centers
434 (see figure 1). Grain size reduction is the result of comminution by crushing.
435 In associtations, grains are increasingly angular and packed. This change causes

436 deformation bands to erode differently than the host sandstone units [37]. De-
 437 formation bands are stronger and more competent to erosion and often protrude
 438 out of outcrop as thin sheets (see figure 2. Unlike the slip surfaces in the area,
 439 deformation bands do not reduce the cohesion of the rock and accordingly do not
 440 have well defined parting surfaces.

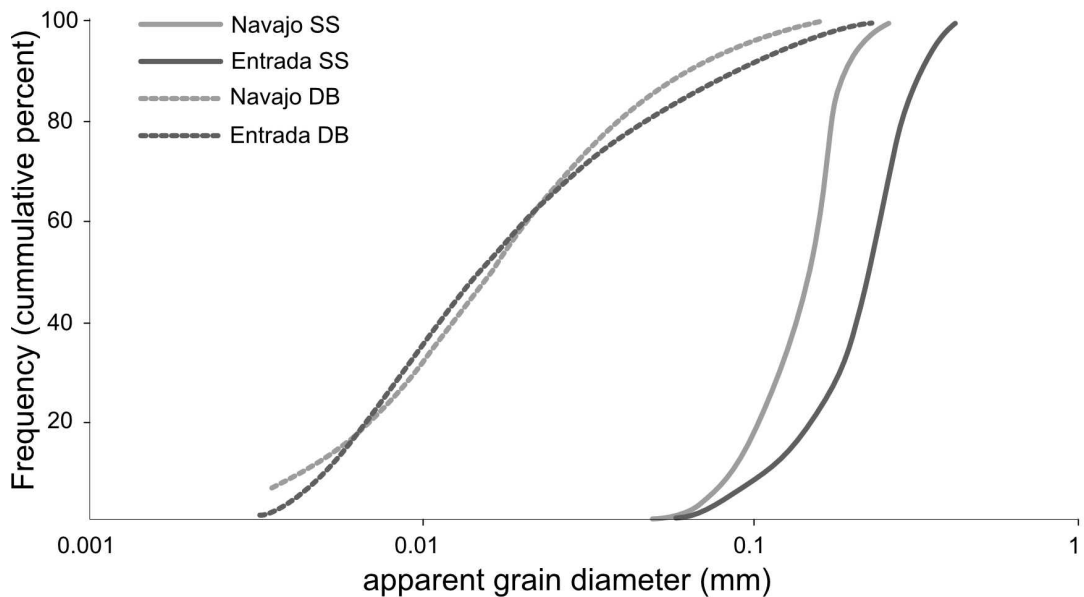


Figure 1: Grains size reduction of crushed grains within deformation bands relative to the undeformed sandstone units, the Navajo and Entrada sanstones. (figure adapted from Aydin, 1978)

441 Deformation bands often outcrop as coalesced nearly co-planar groups or clus-
 442 ters. Deformation band cluster accommodate more intense and localized shear
 443 strain. Larger clusters often have one or many through going slip surfaces. The
 444 clusters are dense networks of anastamozing deformation bands ranging from a few

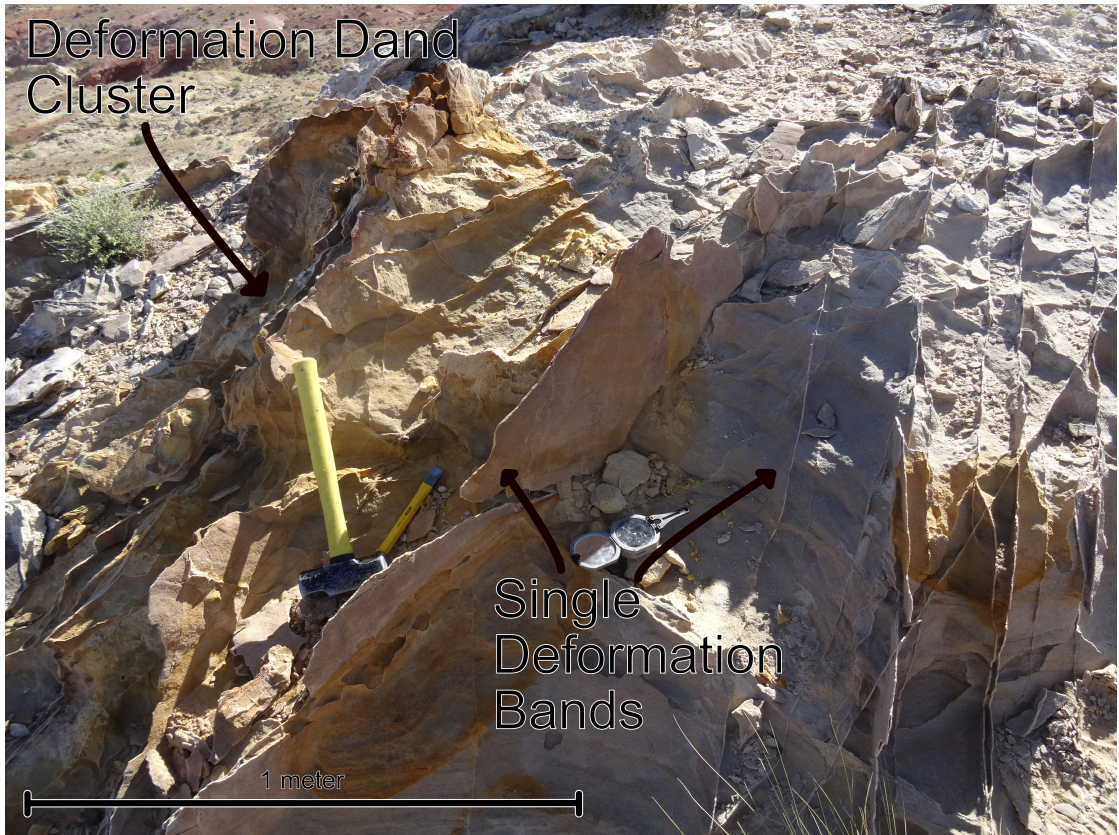


Figure 2: Example of single deformation bands protruding out of outcrop. A small deformation band cluster is also visible in the background.

445 millimetres to tens of centimetres in width, often outcropping as slabs up to meters
 446 in sizes. This erosional feature is most clearly expressed in the Entrada Sandstone.
 447 Clusters commonly form in upright conjugate pairs, each dipping around 60° in
 448 opposite directions.

449 Edges of deformation band clusters that have eroded out appear to have dis-
 450 tinctly corrugated and "lumpy" morphology (see figure 4-left). The orientation
 451 of the corrugations is in clear agreement with the kinematics of through-going
 452 slickensided slip surfaces. The slabs are coated with sand grains from the host
 453 sandstone. There is a clear directional asymmetry along the direction of shear

454 whereby steep faces are in the direction of shear offset and shallowed faces are in
455 the opposite directions (see figure 4). The asymmetry is observed on either side
456 of deformation bands clusters. Refer to Fossen et al., 2007 and Aydin, 1978, for
457 more detailed and very extensive characterizations of defomation bands in these
458 localities.

459 Pre-existing regional joints sets are a common feature of every locality. Joints
460 typically have dips near 90° . Joints set are best defined in the upper Navajo units
461 and low Carmel limestone pavements. The intensity of joint increases near the
462 fault with the occurrence of syn-kinematic sheared and splay joints [31]. Refer
463 to Aydin and Davatzes, 2003, for extensive analysis of joint characteristics and
464 relative timing for each locality.

465 The Entrada unit has more deformation bands and fewer and less well defined
466 joints. Moreover, in the Chimney Rock fault array, there is a clear association to
467 the conjugate fault set orientation. Faults striking



Figure 3: Left: Example of the edge of a deformation bands cluster at Molly’s Castle. Note the ”lumpy” morphology and an clear vertical directional asymmetry. Right: Cross-sectional view of a deformation band cluster with tens of centimeters of shear offset. It is unclear weather there is a through going slip surface localizing displacement. It is , however, definitely not on the edge of the cluster.

⁴⁶⁸ **3.0.2 Slip Surfaces**

⁴⁶⁹ Slip surfaces in the Navajo and Entrada sandstones are most readily identifiable
⁴⁷⁰ by their vitreous polish. Striations and grooves on the slip surfaces mark the
⁴⁷¹ direction of slip. In Cross-section, slip surfaces are discrete, through-going and
⁴⁷² smooth relative to their zero-displacement counterparts. Thin layers, less than
⁴⁷³ a few centimeters in thickness, of milky white layers bound typically bound the
⁴⁷⁴ slip surface. The slip surfaces often cross-cut or bound deformation band clusters.
⁴⁷⁵ For a given slip surface, perpendicular profiles are notably more sinuous than
⁴⁷⁶ slip parallel profiles. Slip surfaces are only preserved in the Navajo and Entrada
⁴⁷⁷ Sandstones. In spite of good exposures in prospecting pits and careful inspection
⁴⁷⁸ of the slip zone, the Navajo-Carmel contact at the Chimney Rock fault array did
⁴⁷⁹ not preserve good surfaces in the Carmel Unit. It is unclear whether this indicates
⁴⁸⁰ that the Carmel units is more susceptible to erosion and/or alteration; or if a
⁴⁸¹ polished finish is only a feature of the quartzite sandstones. Pristine fault slip
⁴⁸² surfaces are not cohesive, and readily form a parting surface. Fresh slip surfaces
⁴⁸³ uncovered *in situ* reveal a relatively consistent meso-structure (see figure – figure
⁴⁸⁴ similar to that in Jamies notes), A sharp interface, separated by a sub-mm thick
⁴⁸⁵ layer of incohesive white powder bounded by two vitreous surfaces is a dense set
⁴⁸⁶ of deformation bands.

⁴⁸⁷ In spite of careful preparation using epoxy, thin sections all parted at the slip
⁴⁸⁸ surface interfaces. Moreover, samples only recording one side of the slip surfaces
⁴⁸⁹ only partially preserved the edge of the slip surface. Thin section observations reveal
⁴⁹⁰ a layered micro-structural architecture of the faults rock locally bound slip surfaces.
⁴⁹¹ The following succession, ordered according to distance from the slip surface is

492 typical for slip surfaces in sand stone: 1) a very fine grained ultracataclastic layer,
493 2) a broader comminuted layer (sometimes absent) and 3) a deformation band
494 zone which grades into the intact protolith.

495 The ultacataclasite is continuous, nearly always bounds the slip surface, and
496 ranges from sub-milimeter to 2 milimeters in thickness. Grain size distribution
497 clearly has a steep fall off with most grains being unresolvable at 400 fold magni-
498 fication. Larger grains are rounded to angular and do not exceed 10's of micron -
499 significantly smaller than protolithic intact grains which are on the order of 100's
500 of micron. Ultra-cataclasite layers show evidence of localized failure (see figure
501 indicative of cycling between healing and brittle failure. Larger survivor grains
502 within the layer are partially offset(see figure xxx). Ultra-cataclasite layers pre-
503 serve a faint foliation oblique to the bounding intact rock. The kinamtics from
504 the flow banding are consistent with sense of shear of grains protruding into the
505 untra-cataclasite and partially sheared off. Previous work has shown no notable
506 change in in the major elements, silicon, calcium, potassium and sodiu, of the
507 undeformed sandstones [4].

508 The broader comminuted layer is not always present. Instead, the fault, still
509 bounded by a thin ultra-cataclasite directly transitions into the intact host. When
510 present, the comminuted layer is onset by a discontinuous interface with layer 1, the
511 fine grained cataclasite. It is evidenced by a distinct change in grain size and spatial
512 arrangement. Past this transition, grains are larger and preserve damaged but
513 intact sedimentary textures from the sandstone. In contrast to the ultracataclasite,
514 the original grain geometry is sometimes still discernible. Grains size within the
515 comminuted layer is spatially variable with bands or lens' of larger grains separated
516 by finer, more angular grains, texturally similar to deformation bands but showing

517 more advanced stages of grain size reductions and shear localizations.

518 The textural transition is best explained by dynamic grain size reduction and
519 wear at the slip surface interface producing ultra-cataclasite which overprint more
520 diffuse off-fault grain size reduction through grain crushing and deformation band
521 production. This layer has highly variable thickness which typically ranges from
522 millimetres to centimetres. Its thickness is asymmetric relative to the slip sur-
523 face. Variability is directly associated to splay features which intensify mechanical
524 damage around the fault. Dark oxide filled fractures up to a few centimetres in
525 length abut steeply into the slip surface and over-print other fault-related textural
526 features. These are characteristically consistent with dynamics tensile cracks and
527 would correspondingly be indicative of seismic rupture velocities.

528 Scattered Electron Microscopy (SEM) reveals

529 Reddish-brown to dark tarnish and reduced vitreous lustres are indicative of
530 advanced erosion. Sections of the slip surface are plucked off. Severely weathered
531 scarps, not scanned in this study, develop a slip perpendicular fabric associated
532 to conjugate fractures and deformation bands abutting into the slip surfaces. In
533 the Chimney Rock Fault Array, lichen grew preferentially on north facing scarps.
534 From our field observation, it is clear that erosion has the effect of re-roughening
535 the slip surfaces, especially at smaller scales. We can confidently attribute these
536 re-roughening effects to erosion because they did not occur in freshly parted slip
537 surfaces.

538 The evolution of slip surfaces with displacement is qualitatively apparent.
539 Faults with small displacements (centimetres of offset) are distinctly different than
540 larger displacement faults (meters of offset). They are 1) visibly more sinuous, 2)
541 laterally discontinuous, 3) less polished, instead, having a dull lustre, and 4) not

542 bounded by well-defined gouge or cataclasites layers bounding the slip surface
543 visible in the field. In spite of extensive investigation, we do not observe faults
544 with well-defined slip surfaces with clear offset markers indicating less than ap-
545 proximately half a centimetre of displacement. It is unclear whether this is the
546 result of an undeveloped reductions in cohesion, as that associated to other slip
547 surfaces observed in the field, or whether it is mechanically favourable to produce
548 deformation bands at such low strain.

549 **3.0.3 Fault architecture**

550 Slickenline orientation of faults in the Navajo and Entrada sandstones indicate
551 normal dip slip with some instances of strike slip offset. Rotation of the slip-
552 direction typically neighbours point of fault intersection [31] [49]. Faults outcrop
553 in relays and cross-cutting conjugate sets. We record dip angles ranging from 44°
554 to sub-vertical with an average dip angle of 70° . The single slip surface accom-
555 modating the bulk of stratigraphic offset is not systematically representative of
556 the fault architecture. Often, fault zones instead have many slip surfaces, sheared
557 joints and splays which partition offset. As is characteristic for high porosity
558 sandstone [5], fault zones all have deformation bands. The intensity of deforma-
559 tion bands rapidly decreases with increasing distance from the fault. according to
560 a power law away from the center of the fault zone and was shown to correlate
561 in intensity with displacement on the fault . Deformation bands typically abut
562 obliquely into the slip surfaces at shallow angles (less than 70°).

563 Certain slip surfaces clearly accommodate the overwhelming majority of fault
564 offset. Displacement accommodated by smaller neighbouring discontinuous slip
565 surfaces is minimal (Shipton, XXX). Based on observations from previous workers

566 and those made in this study where larger displacement slip surfaces are unam-
567 biguously identifiable allowed us to characteristically further its characteristics
568 generalized for the Navajo and Entrada Sanstones as follows:

- 569 • *Large displacement faults are distinctly more discrete and planar.*
- 570 • *Larger displacement faults are not cross-cut by deformation bands or more*
571 *sinuous and discontinuous slip surfaces*
- 572 • *in line with the implicit definition of a fault, the PSS is nearly cohesionless.*
- 573 Locations identified to be expose section of a PSS inevitably cracked open
574 when sampling across the slip surface—the slip surfaces had no cohesion.
- 575 Cohesion is typically thought to reinstate by precipitation and healing. We
576 did not observe recovered healing in this study.
- 577 • *Large displacement faults have a vitreous finish;*
- 578 • *Large displacement slip surfaces are typically in the center of a damage zone.*
- 579 Damage in an inevitable consequence of displacement and the accompanying
580 mismatch that accumulates. Damage at the field locations in this study is
581 expressed as comminution (*e.g.* cataclasite and gouge), fragmentation (*e.g.*
582 breccia, splay joints) and shear deformation (specifically deformation bands).

583 In this study, we refer to *fault rock* as rocks associated to a fault (Snoke et
584 al. 1998). We pay careful attention to the fault rock as it is inevitably coupled
585 to the slip surface roughness and its maturation with cumulative displacement.
586 The faults in our study area display a very diverse range in fault rock lithologies,
587 ranging from fine-grained cataclasites to massive bodies of breccias (up to meters
588 of thickness).

589 Fault rock consistently bounds slip surfaces—often asymmetrically. However,
590 observations at the outcrop scale (10's of meters) both along the strike and dip
591 indicate that both the lithology and thickness of the fault rock are highly heteroge-
592 neous and are subject to large variability. These observations are consistent with
593 more detailed fault architecture mapping conducted by Shipton et al., 2002.

594 We do not observe a clear and tractable relation between fault slip surface
595 displacement and faults rock thickness. This is big part a result of difficulties in
596 defining a clear fault rock thickness criterion which well encapsulates the variety
597 of faults rocks – a challenge well highlighted in (Shipton et al., 2006).

598 * this stuff is left over's from editing and moving things around

599 Healed Gouges - the spot at big hole - iron wash (powder between the surface)
600 - micro-structure - prospecting pit - typically on thinned sections of the fault rock
601 (near the slip surface) Cataclasites - big hole sample with slip surfaces on
602 both sides of the cataclasite - micro-structure - Breccias... - thick sections of
603 the Breccias occur lenses which range from cm's to meters in thickness. Breccia
604 clasts are typically poorly sorted and can be very coarse with clast up to 10 cm
605 in diameter. Clasts show indications for multiple generations of brecciation.

606 Thin Quarts lens - iron wash

607 Systematic associations between fault rock and fault structure exist. For in-
608 stance, Davatzes et al., 2002 reports of a systematic association between the fault
609 rock lithology and the orientation of the fault set. Namely, the orthorhombic fault
610 set striking WNW has systematic association with fragmentation—fault breccias;
611 conversely the ENE fault set rather has slip surfaces cutting through deformation
612 band clusters (see figure ??). This relation was speculated to be the result of
613 contrasting genetic mechanism. The WNW set is the result of the reactivation of

614 regional joints. In contrast the ENE fault set is the the result of clustering and
615 anastamosing deformation bands acting as a catalysing agent to the formation of a
616 faults. In this study, we observe clear instance of lithological contacts being asso-
617 ciated to brecciation (photo at iron wash where the top of the Navajo is brecciated
618 and quickly reverts to a single fault strand. More over, large breccia bodies are
619 clearly related to points where faults are cross-cutting each other at high obliquity
620 as is often the case at the Chimney Rock fault array and

621 Complicating factors:

622 Associations between brecciation and lithological contacts...

623 Associations between brecciation and cross cutting faults...

624 For an extensive review and description of the faults in the Navajo and Entrada
625 sand stones refer to Aydin's thesis.

626 **3.1 Interpretation of field observations and roughness mea- 627 surements**

628 Cross-cutting relationships reported bot in this study and in previous work on
629 faults in the Navajo and Entrada units of the San-Rafael swell are particularly
630 informative. Large displacement slip surfaces are not cross cut by deformation
631 bands and more sinuous slip surfaces. However, large displacement slip surfaces
632 do cross-cut clusters of deformation bands and more sinuous slip surfaces. This re-
633 lationship is indicative of a clear evolution of the fault architecture by 1) localizing
634 displacement and 2) smoothing out slip surfaces.

635 Faults zones with larger offset are associated to larger damage zones and more
636 slip surfaces. This is particularly telling fact when with the observation that small

637 displacement slip surface do not cross cut larger displacement slip surfaces.

638 The cross cutting relationship implies that either slip either smaller less con-
639 tinuous slip surfaces predate the onset of the larger offset slip surface or that the
640 they splay off of it. However, we can reject the former as a possible mechanism as
641 it does not account for the increased density of slip surfaces on larger offset fault
642 zones. This implies that they either form directly from the stress heterogeneities
643 induced by the roughness of larger displacement slip surfaces.

644 Slip surfaces pre-dating large The former case stress heterogeneities from active
645 slip surfaces induced by fault roughness.

646 faults are smoother than joints or deformation bands

647 At the grains scale, grains are truncated, not ‘plucked’.

648 more linear fault traces where not offset by wavier fault traces

649 **4 Geometric analysis**

650 **4.1 Method**

651 This study focuses on the qualitative and quantitative evolution of fault slip sur-
652 faces—both addressing how fault slip surfaces evolve and the implications thereof.
653 The quality of the displacement measurements and the large number of accurate
654 surface scans are fundamental to the quantitative analysis of the data. Field-
655 method and data acquisitions thus reflect these standards.

656 For the qualitative analysis, we carefully record the characteristics of the fault
657 architecture in the context of fault evolution. Specifically, we are particularly
658 meticulous about 1) identifying cross-cutting relationships which indicate temporal

659 evolution on the on fault, 2) identifying the evolutionary stages in the formation
660 of faults and 3) identifying and characterizing the wear product, or fault rock,
661 produce as faults evolve.

662 For the quantitative analysis, we collect scans both *in situ* and from hand
663 samples collected in the field. Scans are associated to a constraint on displacement.
664 Moreover, for every scan, the time of day, location, quality, strike and dip of the
665 fault slip surface as well as the rake of the slickenlines are recorded. When possible
666 we record an estimate of the fault rock thickness. Finally, we also record both a
667 plan and cross-sectional view image of the scanned fault surfaces. See appendix
668 for the tabulation of this data. Together, all these measurements and observations
669 should provide the necessary data to robustly explain and quantify the process
670 through which faults mature.

671 4.1.1 Scan Data Acquisition

672 To measure slip surface roughness, we analyses large point clouds scans of real
673 fault surfaces and average the slip parallel and perpendicular spectral and statis-
674 tical properties across hundreds of profiles. Point clouds must be obtained across
675 a flexible array of instruments to properly capture the fractal scaling behavior
676 (Brown and Scholtz, 1985; Candela et al., 2012). In this study, we use three in-
677 struments with complimentary scales of observation. Together, these instruments
678 offer accurate and precise three-dimensional discretization of fault surfaces at over
679 nine decades of length scale.

680 *make a map of each areas with the location of every scan encoded with dif-
681 ferent symbols*

682 At the largest scales ranging from meters down to millimetres, a light detection

and ranging instrument (i.e. LiDAR). We use the LiDAR has been used in many previous studies of fault roughness as it is easily deployable in the field and provides rapid means to collet very large point cloud data set. However, its use is limiting as it requires exceptionally good and, accordingly, rare exposure of fault surfaces that are large enough and fresh enough to not have been degraded by erosion. In this study, we report 5 ??? Lidar Scans (see figure).

Instead, the bulk of in situ field measurements were made at intermediate scales ranging from centimeters down to hundreds of microns with the NextEngine 3D laser scanner. The NextEngine laser scanner is accurate down to 100 microns with resolution up to 41 540 points per square centimeter. Note that the NextEngine is a much less cost prohibitive option when compared to the LiDAR yet captures the same characters of the fault surfaces. The laser scanner was benchmarked to a machined-flat granite surface and to a scan of the corona slip surface both to industrial-grade laser scanner as reference. The scanner is not exactly built to be field ready. It requires a power source, low light conditions, a stable surface to sit on, limited dust exposure and must be connected to a computer. Moreover it only allows for a very limited depth of field. To use the scanner in the field, we connected both the laser scanner and laptop to a solar powered, *goal zero*, battery. The scanner was encased and padded in a reinforced cardboard box with its depth exactly equivalent to the optimal depth of field. The set up had the added advantage of being very portable, completely removing sunlight and limiting dust exposure. We report XXX scans using the NextEngine Laser scanner.

Finally, hand samples were collected and analyzed with the Zygo blah blah, an optical profilometer enabling accuracy from milimeters down to sub-micron. The Zygo blah blah uses white light interferometry to produce relatively small

708 point-clouds (XXX points) at various magnifications. It does however allow for
709 seamless stitching of scans. Individual and stitched scans using the profilometer
710 were benchmarked to a silicon carbide reference machined flat to XXX meters.
711 All samples were scanned at 20x magnification and stitched together to produce
712 sections roughly XXX by XXX millimeters. In addition, samples were scanned
713 at the lowest magnification to properly bridge the gap up to the laser scanner
714 resolution. We report scans of XXX samples with the white light profilometer,
715 XXX of which were taken from surfaces scanned in the field with the laser scanner.

716 **4.1.2 Constraining displacement**

717 We associate every scan with a displacement constraint. At The Chimney Rock
718 Fault Array and Big Hole Fault entire displacement profiles have been measured
719 during previous mapping campaigns (i.e. Maarten shipton). At Iron wash, Horse
720 Creek and Molly's Castle, Atilla Aydin's mapping identified clear offset markers
721 where available. Base maps for all field locations were georeferenced using satellite
722 images when necessary and used as a reference in the field to streamline scan data
723 acquisition. Displacement was estimated after the field campaign using GPS
724 locations collected in the field. Additional measurements using basic tape measure
725 and compass triangulation methods were also obtained in the field.

726 Base maps only report stratigraphic throw or, in some cases, offset across *entire*
727 fault zones. However, many slip surfaces, complex networks of deformation bands
728 and sheared joints which partition offset across fault zone (see figure). We
729 therefore make a distinction between *offset* across an entire fault and *displacement*
730 across a single slip surface. Without good marker horizons and cross-sectional
731 exposure, stratigraphic offset is accommodated across slip surfaces is ambiguous.

732 Offset across the entire fault zone therefore only serves as an upper-bound con-
733 straint on displacement across a single slip surface slip surface. In XXX of XXX
734 fault slip surface measurements, this is the best available constraint on displace-
735 ment.

736 PUT THIS UNDER FIGURE "At Big Hole fault, two large-scale continuous
737 strands of the fault, both accommodating meters of displacement exemplify this
738 mechanism at a larger scale. In accordance, Shipton and Cowie, 2003 report large
739 uncertainty on the partitioning of stratigraphic offset across the two strands".

740 We were able to reconstruct exact displacement in the following specific cases:
741 1) If full cross sectional exposure indicates a single slip surface; 2) If cross-sectional
742 exposure is good enough to clearly indicate an offset marker (lamella, cross-bedding
743 or lithological contact) and its attitude, traceable to the slip surface exposure;
744 or 3) if it is unambiguous that one principle slip surface is accommodating an
745 overwhelming majority of fault offset, i.e. it is continuous, it has a layer of fault
746 rock and unmistakably more linear and sharp than any other slip surface in the
747 fault zone.

748 Errors on displacement estimates are either reported directly for previous work
749 (i.e. 1m precision for Maerten's throw measurements and 5m for Shipton's off-
750 set estimates) or conservative 10% error on displacement estimates measurements
751 made directly in the field.

752 *make a table regarding the different types of displacement constraints*

753 known unknown equation assumptions N

754 - throw - assuming 60 deg dip, dip slip - throw, dip – assuming dip slip -
755 throw, dip, rake – assuming constant displacement orientation - direct off-set –
756 with different permutations . . .

757 **4.1.3 Scan data Processing**

758 I use point cloud spatial statistics to characterize and quantify active surface pro-
759 cesses on faults. I developed a *MatLab* work flow to entirely automate data pro-
760 cessing from the raw *.xyz* input format to the final statistical analysis:

761 1. Preprocessing

762 (a) manual inspection for coarsest defects

763 (b) Import *.xyz* data into *Matlab*

764 (c) Very coarse Height field filter

765 (d) Flatten points

766 (e) Grid data

767 (f) Orient grid along slip direction (using power spectral analysis

768 (g) Remove defects

769 i. Remove outliers in the height field

770 ii. Fractal model filter

771 iii. Remove abnormally flat (interpolated) sections

772 2. Processing

773 (a) Statistical analysis

774 i. Scale dependent *RMS*

775 ii. Scale dependent skewness

776 iii. Scale dependent kurtosis

777 iv. Scale dependent asymmetry

778 (b) Spectral Analysis

779 i. Fast Fourier Transform (FFT)

780 ii. Lomb-Scargle Periodogram

781 *make into figure, include bypasses and other recent additions*

782 Note that the general pre-processing workflow was slightly adapted according
783 to the different instruments that where used in the study. These adaptation were
784 mostly attributable to the quality of the data at the various scales of acquisition
785 and the actual instrument specifications. Scans collected with the LiDAR required
786 more extensive manual point removal to avoid features such as vegetation, spurious
787 outlier and large defects to affect the quality of the preprocessing. Scans collected
788 at the intermediate scale with the laser scanner easily followed this workflow.
789 Finally, scan collected with the white light interferometer did required minimal
790 preprocessing and where aligned manually at the time of data collection.

791 Before conducting a statistical analysis scan data must be pre-processed into a
792 workable format. Scan data is a point cloud - a series of points with coordinates
793 x , y and z . Scans reported in this study typically have 10^6 to 10^7 points. In raw
794 form, the point clouds are randomly oriented, noisy and still contain instrumental
795 and physical artefacts. Physical artefacts include cracks, eroded sections, and
796 vegetation; instrumental artefacts include noise, smoothing and scattering. All
797 these features must be removed. The process of manual removal is labour intensive
798 and unfeasible for a data set of the scope presented in this study. I rather opt to
799 automate this process. Only very large defects (defects that may substantially
800 effect the quality of finding a true mean plane) are manually removed.

801 The surface must first both be flattened and aligned along slip. Linear trends

802 in the data induce an unwanted high frequency signal in data and also affect the
 803 quality of later interpolation onto a grid. Thus, x , y , z data is rotated using
 804 around the axis \mathbf{u} as determined by the normalized cross product between the
 805 surface normal \mathbf{n} and a vector normal to a flat surface ($\mathbf{n}_2 = [001]$):

$$\mathbf{u} = \mathbf{n} \times \mathbf{n}_2 / |\mathbf{n} \times \mathbf{n}_2|$$

806 with the rotation,

$$R = \cos \theta \mathbf{I} + \sin \theta [\mathbf{u}]_x + (1 - \cos \theta) \mathbf{u} \otimes \mathbf{u},$$

807 were $[\mathbf{u}]_x$ is the cross product matrix of u and \otimes is the tensor product and I is
 808 the identity matrix.

809 Fault surfaces are anisotropic. The direction of slip is preserved in the anisotropy
 810 whereby the 'smoothest' direction is slip parallel and the 'roughnest' direction is
 811 perpendicular to slip. The fault scan is rotated around the z axis such that the
 812 direction of slip is along the x axis. The direction of slip is by decimating raw data
 813 before iteratd steps of regridding, one-degree rotation and spectral analysis. In
 814 the radial search, roughness is quanified as the integral of the log-weighted power
 815 spectrum over the entire bandwidth of the sample surface. The angle associated
 816 to the minimum in roughness is then identified as the direction of slip and sub-
 817 sequently used to rotated the original flattened point cloud. The data is then
 818 interpolated onto a grid using a linear interpolation algorithm. The point spacing
 819 is automatically defined by the point density over the areal extent of the data:

$$\Delta x = N_{pts} / AXXXXXX \quad (7)$$

820 INCLUDE HISTOGRAMS FOR EACH FILTER

821 *Defects* include all physical surface features that are clearly not associated
822 any faulting process, *e.g.* cracks, eroded patches, vegetation, etc.. Defects are
823 identified and filtered out using combination of thresholding methods. These
824 methods all revolve around identifying clear points or segments that are statistical
825 outliers to the distribution characterizing the entire surface—abnormal points.

826 The most aggressive filter implemented searches for outliers to the fractal
827 model. The filter removes entire linear segments with abnormally high variance
828 in the height field for the given scale of observation. For this implementation, I
829 iterate over 10 filter scales. The scales are selected using a log spacing from the 10
830 points up to the length of the entire surface. The threshold for segment removal
831 is chosen to be four standard deviations from the mean (should account for < 0.1
832 percent of the data in a normal distribution). Note that, assuming a normal distri-
833 bution of variance data for a given scale, the filter should not induce a systematic
834 bias since the filtering is symmetric around the mean. However, surface features
835 associated with a truly distinct mechanism of formation, in this case cracks and
836 other defects that will typically have much higher variance, *are* be removed. This
837 general approach ensures that defects, regardless of their scale get identified and
838 removed. This is important for any subsequent fractal analysis.

839 Abnormally flat sections arise as the result of triangular interpolation of sparse
840 points. Typically, interpolation on the edge on a non-convex set of points is subject
841 to this effect. These artefacts are readily identified in the curvature data. In the
842 log-transformed absolute value curvature field, these sections appear to be nearly
843 or exactly zero. The filter rejects point with curvatures less than 10^{-25} . These
844 values likely associated to the linear interpolation scheme.

845 Finally, all scan are inspected to make sure that the pre-processing was suc-
846 cessful. The script fails to properly process scans that are excessively populated
847 with surface defects. These scans were manually cleaned and oriented before re-
848 processing them. Manual changes were executed in *CloudCompare*.

849 Pre-processed scans are N by M scalar fields of fault surface topography(the
850 sitance from the mean plane) aligned with slip along the x axis. NaN values mark
851 locations where data is missing or was removed by filters. Point spacing is defined
852 the mean point density of the scan in the x - y plane.

853 **4.1.4 Statistical Analysis**

854 After pre-processing, scans discretize defect-free slip surfaces with grids with rows
855 aligned with the slip direction. We compute the power spectral density content for
856 every continuous segment of every single profile of the grid using a Fast Fourier
857 Transform (FFT). Individual spectra are interpolated onto a master frequency
858 vector. For a given frequency, the distribution of power values across the pro-
859 files through along the slip is strongly skewed (see figure xxx). The skewness is
860 attributable to the non-negative constraint on power and residual outlying pro-
861 files (defects not properly removed). To provide a more representative and robust
862 measure of maximum likelihood, we use the geometrical mean instead of the arith-
863 metical mean. Accordingly, errors represent the 1σ range in the log-transformed
864 distribution. The analysis yields one representative spectrum for each scan.

865 The spatial frequency content of slip surfaces follow a power law. This charac-
866 teristic is roughly fixed for a single slip surface regardless of the scale sampled in
867 our instrumental array. Fixed scaling and its power law form in frequency space is
868 a feature of the fractal character of fault surfaces. We can thus further distil the

869 roughness measurements using the fractal model of the fault:

$$P(k) = Ck^{-\beta} \quad (8)$$

870 Accordingly the entire spectral information of a scan can be summarized with
871 the prefactor (C) and the scaling exponent (β). Determining fractal parameters
872 from spectra is not trivial. *A priori*, the fractal model is determined using a
873 weighted power law regression through the spectra. Weights are determined ac-
874 cording to the inverse $1\sigma^2$ variance of the power estimates. However, confidence
875 interval on the fit parameters are strongly sensitive to both instrumental and an-
876 alytical biases (XXX schittbulh 1998). Biases induce unwanted high or low pass
877 filters in the spectral content-amplifying or diminishing selective bandwidth. The
878 combination of instruments and highly overlapping bandwidths provides a means
879 to identify the affected sections and suppress methodological bias. The comparison
880 of the power law fit through multiple heavily overlapping instrumental bandwidths
881 to the representative spectral of individual scans highlights instrument-specific bi-
882 ases. In doing so, we identify conservative bounds on sections of frequency spec-
883 trum that deviated from the power law fit. For our instruments, we find that
884 artefacts are particularly disruptive at the small scale instrumental limit. The
885 LiDar and laser scanner are dominated by a shallower slope at the high frequency
886 tail of the spectra which has been interpreted in previous studies as random noise
887 (XXX). Conversely, the spectra of the scan collected using the white light interfer-
888 meter have steeper high frequency tails. This artefact has not been reported in
889 previous studies in spite of the extensive use of the instrument. This discrepancy
890 is likely attributable to the comparatively limited and subdued use of aggressive

smoothing filters both in the scan data and in the spectra our analysis. Affected bandwidths are omitted from subsequent analysis. In spite of this approach, small discrepancies in parametrization of the power law fit for a given slip surface render the extrapolation of measurements from on instrumental bandwidth to the other instrumental scale of limited use. We therefore choose to report any further results at the bandwidth or specific wavelength best captured by the instrumental magnification.

INCLUDE A FIGURE WITH: ORIGINAL SURFACE, AUTOMATICALLY PROCESSED GRID, MANUALLY PROCESSED GRID AND CORRESPONDING POWER SPECTRA.

identifying fractal scaling section plot of white light all magnifications computational scheme to select the good section error on direct displacement estimates?

4.2 Results

4.2.1 Roughness measurements

figures to include:

- all spectra
- increasing anisotropy (two surfaces) - polar plot

Figure XXX shows the all the PSD calculations obtained from the scans collected in this study. Consistent with previous work, we find that the PSD spectra over the entire bandwidth reported in this study generally follow a power law scaling (a linear relation in log-log space). This feature corresponds to the constant fractal scaling. The scaling exponent and pre-factors are calculated using linear

913 least-squares fit of the spectra in log-log space. The Hurst exponent can then be
914 obtained according to equation XXX.

915 In the slip perpendicular direction, Hurst exponents range from XXX to XXX,
916 with an average value of 0.8ish; Prefactors range from XXX to XXX with an
917 average value of XXX. In the slip parallel direction, Hurst exponents range from
918 XXX to XXX, with an average value of 0.8ish; Prefactors range from XXX to
919 XXX with an average value of XXX. Implicit to the pre-processing grid alignment,
920 for any single scan the slip parallel direction is systematically smoother than the
921 slip perpendicular direction indicating a clear surface anisotropy. The entire data
922 set does however indicate an overlapping range in slip parallel and perpendicular
923 directions. We also note that lower pre-factors are generally associated to lower
924 Hurst exponents.

925 An evolution with displacement is weakly expressed in the spectral analysis but
926 is cluttered and obscured by highly variable errors on displacements and rough-
927 ness measurements. In order to highlight the effect of displacement on the sur-
928 face roughness, we separate our scan data into two distinct populations. 1) Scan
929 data with direct displacement constraint and 2) scan data associated to maxi-
930 mum displacement constrains. Brodsky et al., 2011, tested the validity of a power
931 law relation between fault roughness are various specific scales and displacement.
932 Building upon this approach, we use both data populations to test the validity
933 and parametrization of the fit and the Implicit hypothesis that faults smooth as
934 a function of displacement—the smoothing model. Scan data with direct displace-
935 ment constraints serves as a direct test and a means to parametrize the smoothing
936 model. For the model to be valid it must agree with further constraints imposed
937 by data with only maximum displacement estimates.

938 A point defined by the maximum error bound on displacement and the rough-
939 ness of the fault surface is in agreement with smoothing model if it is rougher
940 than roughness prescribed by the model as parametrized by direct measurement.
941 Conversely, if the point is rougher than the model prediction, it is not physically
942 possible in the model construct. A null hypothesis would prescribe no bound on
943 the roughness and would simply have the predicted roughness of a fault be defined
944 by the probability distribution function of the entire roughness dataset.

945 * probably will revisit this *

946 Accordingly, we can roughly estimate the probability that our distribution of
947 data relative to the smoothing model is a random element of chance according to:

$$P = \prod p(y_i > Y(x_i)) \quad (9)$$

948

949 Figures XXX to XXX shows the relation between roughness and displacement
950 as interpolated a various scales of observation. Vertical error bars on the power
951 spectral density are obtained from the confidence interval of the of the fractal
952 model regression. Horizontal errorbars on displacement are defined on a case by
953 case basis from field observations and previous work in on the fault arrays. We
954 present both the fit through the our entire dataset (comprised of direct and up-
955 per bound constraints on displacement) and through the the directly constrained
956 displacement estimates. Fits are obtained using a least squares linear regression
957 through the log-transformed data sets. In order to provide error bounds on the
958 fit parameters, we use a full Monte Carlo simulation sampling direct displacement
959 estimated as Gaussian distributions, upper bound displacement constrains as com-

960 pletely random distributions across the entire possible range of displacements and
961 power spectral density estimates as log normal distributions. Errors represent on
962 standard deviation estimated from 10000 simulations.

963 The weak trend across the entire dataset imply and expectation of smoother
964 slip surfaces in fault zones which have accommodated larger displacement.

965 Conversely the stronger trend across the well constrained data implies that an
966 individual slip surface smooths with displacement. The smoothing exponent varies
967 according to the different scales of observation (XXX at the laser at the centimeter
968 scale, XXX at the milimeter scale and XXX at the micron scale). While a power
969 law fit to the best constrained measurements is has poor fit metrics, we find a
970 nearly perfect agreement with roughness measurements only associated to upper
971 bound constraints.

972 Two constraints on displacement – two data populations plot of all the spectra
973 color coded with displacement smoothing plots: parallel - ζ all scales perpendicular
974 - ζ all scales Hurst exponent - ζ all scales Fit for smoothing through direct data,
975 discuss consistency with max disp data Other statistical metrics? Poly-gaussian
976 features in the surface roughness Skewness of height field as a function of scale
977 Null result worth reporting? Do a plot of the evolution of skewness at the grain
978 scale?

979 qualitative illustration of maturity

980 4.3 Hard facts

981 The following is a list of ‘hard facts’ that can be established from the both the
982 qualitative and quantitative data:

- 983 • faults are smoother than joints or deformation bands
- 984 – power spectrum shows that fault slip surfaces are systematically smoother
- 985 that joint and deformation band surfaces at all wave lengths reported
- 986 in this study (10^{-6} to 10^5 meters)
- 987 • At the grains scale, grains are truncated, not ‘plucked’.
- 988 • The roughness of a slip surface is sensitive to its displacement history. This
- 989 result is robust across multiple faults both nucleated from deformation bands
- 990 and joints and variations in fault rock and host rock lithology.
- 991 • The smoothing exponent is likely more than 1 at certain scales - quote from
- 992 Emily: “In all of these cases, the scatter of the data is large, but the basic
- 993 result holds: the absolute value of the exponent is much less than 1.”
- 994 • The smoothing rate is highest at small displacements and decreases with
- 995 displacement.
- 996 • Smoothing occurs at all scales of this study
- 997 • a slip surface from a large offset fault is more likely to be smoother
- 998 • for any given the displacement on a fault, the smoothest slip surface roughly
- 999 follows the same smoothing trend as that defined by direct displacement
- 1000 measurements.
- 1001 • The roughness varies spatially on a slip surface - the scatter in the data
- 1002 exceeds the instrumental error

- 1003 • the height distribution of points on a slip surface can be far from normally
1004 distributed.
- 1005 • the Hurst exponent has a very large range in values (less than Zero to 0.9)
- 1006 • more linear fault traces where not offset by wavier fault traces

1007 5 Model

1008 In this study, we utilize work minimization and boundary element numerical mod-
1009 elling to capture the growth of fault damage and the effect of rough asperities.
1010 The modelling component is motivated by the following questions: can geomet-
1011 rical asperities fail through shear? In so doing, how do they fail?—and what are
1012 its sensitivities to asperity geometry and strength? Does strength heterogeneity
1013 and mechanical wear by the truncation of asperities properly capture the evolu-
1014 tion of fault slip surfaces with displacement. These questions prompt the need for
1015 physically robust models that can be accomodating of complex fault or asperity
1016 geometries. The complexity of these geometries imply that off fault damage will
1017 grow in complex stress conditions— conditions that are currently poorly captured
1018 by simple analytical solutions (e.g. [26]). Moreover, complexities related to the
1019 discontinuous nature of fracture are more simply captured by boundary element
1020 modelling than existing finite element or finite difference models. This simplicity
1021 arises from need of fewer, less sparse, sets of equations to solve ([30]). Limita-
1022 tions of the boundary elements approach for fault modelling and off fault damage
1023 predictions is the difficulty of accumulating offset. Maximum allowable offset is
1024 roughly half the length of boundary elements. Along with this complications is the

1025 implicit trade off between model resolution and displacement. Approaches can be
1026 taken to circumvent the challenge however its development and implementation
1027 are beyond the current scope of this study.

1028 The model builds off of fric2D and growth by optimization of work (GROW)
1029 developped by Michele Cooke and Jessica McBeck. Fric2D solves for displacement
1030 and stress conditions on fault elements with prescribed constitutive behaviours
1031 given prescribed boundary element stress boundary conditions and material prop-
1032 erties in two dimensions. Constitutive behaviour of fault elements are defined by its
1033 static and dynamic friction, critical slip distance, and shear and normal stiffness.
1034 In turn the behaviour of the medium fault elements and boundary elelements is
1035 linear elastic defined by Poisson's ratio and Yougn's modulus. For its part, GROW
1036 predicts fracture propagation paths. It does so by minimizing the external work on
1037 a system. As a natural analogue, the external work is the tectonic work imposed
1038 on a fault and its fault blocks, together comprising the system. The model allows
1039 for the simultaneous growth of multiple fractures. The general algorithm uses the
1040 same boundary element method as fric2D to describe the fractures–linear dislo-
1041 cation elements that discretize the entire length of the fault. As a crack grows,
1042 dislocation elements are added radially to the tip of the crack so as to minimize the
1043 external work on the system normalized by the crack area ($W_{ext}/\Delta A$). External
1044 work is further defined as:

$$W_{ext} = \oint (\tau u_s + \sigma_n u_n) dB \quad (10)$$

1045 External work is readily calculated from the the output of fric2D. Accordingly
1046 it is possible to iteratively test a range of directions of growth, compared the

1047 external work required, and choose the energetically preferred direction of crack
1048 growth. This process continues until stress at the tip of the cracks is not sufficient
1049 to overcome the fracture toughness. Therein lies the general algorithm of GROW.

1050 In practice GROW utilizes almost the same inputs as fric2D. The user must
1051 specify what points are considered to be 'flaws'. Only the coordinates associated
1052 to the flaws are analysed and allowed to grow according to the GROW algorithm.
1053 The computational cost of multiple initiation points is large. Every added flaw
1054 grows the computational cost exponentially according to the angular range and
1055 resolution. We rather use fric2D to educate the choice of coordinated for the flaws
1056 on the fault.

1057 Stress conditions are assessed along the fault elements. Normal (σ_{11}), shear
1058 ($\sigma_{12} = \sigma_{21}$) and tangential (σ_2) stresses on the fault elements yield the two di-
1059 mensional stress tensor. Its Eigenvalues in turn allow for the determinations of
1060 principle stresses (σ_1 and σ_3). These in turn allow for calculation of the Mohr
1061 Coulomb stress and the assessment of elements prone to failure in shear according
1062 to host rocks angle of internal friction (ϕ) and cohesion (c).

$$\tau_m = \sigma_m \sin(\phi) + c \cos(\phi) \quad (11)$$

1063 where,

$$\tau_m = \frac{\sigma_1 - \sigma_3}{2} \quad (12)$$

1064 and,

$$\sigma_m = \frac{\sigma_1 + \sigma_3}{2}. \quad (13)$$

1065 We also assess element that may fail in tension. Elements with least principle
1066 stress in tension exceeding the cohesive strength of the medium are also identified
1067 as being prone to fail. In the likely case that entire fault segments (multiple fault
1068 elements) are in stress conditions exceeding the failure criterion of the rock, we
1069 choose local maxima of Coulomb stress and tensile stress along these segments as
1070 the failure points.

1071 This additional functionality is implemented in Matlab and seamlessly links
1072 fric2d, failure assessments and GROW into one single workflow.

1073 **5.1 Model Results**

1074 **6 Discussion**

1075 **6.0.1 Tying the model together with roughness measurements and** 1076 **model**

1077 wear rate (character), tying together model with

1078 **6.1 An external estimate of gouge production and fault** 1079 **thickness * this section will likely be removed**

1080 The data collected in this study offers the unique opportunity to provide new
1081 indirect estimates of fault rock production, fault thickness and dilation rate over
1082 an entire fault. We know that 1) the primordial roughness is systematically rougher
1083 than mature faults, 2) the primordial roughness is relatively constant, and 3) the
1084 roughness can be estimated for a given displacement. Using these results, I will
1085 estimate the volume of fault rock produced through wear and the corresponding

1086 roughness induced accomodation space in the fault system.

1087 Displacing two rough fractal surface in shear requires dilation. The expectation
1088 dilation can be estimated according to the amplitude of the largest wavelength (λ)
1089 being offset (see figure XXX). For a given displacement, u , the largest wavelength
1090 in the system will be $\lambda = 2u_i$. Using a fractal paradigm to define the average
1091 amplitude of a given wavelength according to the pre-factor β and the Hurst
1092 scaling exponent, H , (*reference the equation*) we find that the dilation, A can
1093 be expressed as a function of displacement:

$$A(u) = \sqrt{\beta 2u^{-2H-1}} \quad (14)$$

1094 If we apply this to an entire fault system with displacement field, U , we can
1095 estimate the void space that would be produced:

$$V_{void}(U) = \int_S \sqrt{\beta 2U^{-2H-1}} dS \quad (15)$$

1096 Since the fault system is closed any change in fault roughness *must* be coupled
1097 to the fault core. If all changes in the fault surface are associated to a production
1098 of fault rock, we can effectively estimate the volume of fault rock that has been
1099 produced from diplacement u_0 to u_f by comparing the volume integral under the
1100 corresponding initial and final slip surfaces $S(u_0)$ and $S(u_f)$.

$$\frac{\Delta V_{faultrock}}{\Delta u} = \int_S S(u_0) - S(u_f) dS \quad (16)$$

1101 volume integral under the surfaces, S , can be estimated numerically according
1102 to the frequency distribution prescribed by the RMS the entire fault system. Note

₁₁₀₃ that the RMS is estimated at the length scale of the entire fault; wear processes
₁₁₀₄ are active at all length scales below this.

$$\int S dS \approx \quad (17)$$

₁₁₀₅ Now for the displacement field, U , we can estimate the total fault rock produced
₁₁₀₆ by using the primordial surface roughness, $S(0)$, and the prediction of the surface
₁₁₀₇ roughness extrapolated to the length of the fault (* reference the the equation of
₁₁₀₈ smoothing *) such that:

$$V_{faultrock}(U) = \int_S S(0) - S(U) dS \quad (18)$$

₁₁₀₉ The comparison between the two quatities is telling. If the amount of fault
₁₁₁₀ rock is

₁₁₁₁ 7 conclusion

₁₁₁₂ 7.1 future work

₁₁₁₃ References

- ₁₁₁₄ [1] Keiiti Aki. Asperities, barriers, characteristic earthquakes and strong motion
₁₁₁₅ prediction. *Journal of Geophysical Research: Solid Earth*, 89(B7):5867–5872,
₁₁₁₆ 1984.
- ₁₁₁₇ [2] JeFoa Archard. Contact and rubbing of flat surfaces. *Journal of applied
1118 physics*, 24(8):981–988, 1953.

- 1119 [3] CA Aviles, CH Scholz, and John Boatwright. Fractal analysis applied to char-
1120 acteristic segments of the san andreas fault. *Journal of Geophysical Research: Solid Earth*, 92(B1):331–344, 1987.
- 1121
- 1122 [4] Atilla Aydin. *Faulting in sandstone*. PhD thesis, Stanford, 1977.
- 1123 [5] Atilla Aydin and Arvid M Johnson. Development of faults as zones of defor-
1124 mation bands and as slip surfaces in sandstone. *Pure and applied Geophysics*,
1125 116(4):931–942, 1978.
- 1126 [6] Nir Badt, Yossef H Hatzor, Renaud Toussaint, and Amir Sagy. Geometrical
1127 evolution of interlocked rough slip surfaces: The role of normal stress. *Earth and Planetary Science Letters*, 443:153–161, 2016.
- 1128
- 1129 [7] Philip Berger and Arvid M Johnson. First-order analysis of deformation of a
1130 thrust sheet moving over a ramp. *Tectonophysics*, 70(3-4):T9–T24, 1980.
- 1131 [8] RL Biegel, W Wang, CH Scholz, and GN BorrNoTr. 1. effects of surface
1132 roughness on initial friction and slip hardening in westerly granite. *Journal of Geophysical Research*, 97(B6):8951–8964, 1992.
- 1133
- 1134 [9] Andrea Bistacchi, W Ashley Griffith, Steven AF Smith, Giulio Di Toro,
1135 Richard Jones, and Stefan Nielsen. Fault roughness at seismogenic depths
1136 from lidar and photogrammetric analysis. *Pure and Applied Geophysics*,
1137 168(12):2345–2363, 2011.
- 1138 [10] Elisabeth Bouchaud. Scaling properties of cracks. *Journal of Physics: Con-*
1139 *densed Matter*, 9(21):4319, 1997.

- 1140 [11] Frank Philip Bowden and David Tabor. *The friction and lubrication of solids*,
1141 volume 1. Oxford university press, 2001.
- 1142 [12] Emily E Brodsky, Jacquelyn J Gilchrist, Amir Sagy, and Cristiano Collettini.
1143 Faults smooth gradually as a function of slip. *Earth and Planetary Science
1144 Letters*, 302(1):185–193, 2011.
- 1145 [13] Emily E Brodsky, James D Kirkpatrick, and Thibault Candela. Constraints
1146 from fault roughness on the scale-dependent strength of rocks. *Geology*,
1147 44(1):19–22, 2016.
- 1148 [14] Stephen R Brown and Christopher H Scholz. Broad bandwidth study of the
1149 topography of natural rock surfaces. *J. geophys. Res*, 90(B14):12575–12582,
1150 1985.
- 1151 [15] Roland Bürgmann, David D Pollard, and Stephen J Martel. Slip distribu-
1152 tions on faults: effects of stress gradients, inelastic deformation, heteroge-
1153 neous host-rock stiffness, and fault interaction. *Journal of Structural Geology*,
1154 16(12):1675–1690, 1994.
- 1155 [16] J Byerlee. Friction, overpressure and fault normal compression. *Geophysical
1156 Research Letters*, 17(12):2109–2112, 1990.
- 1157 [17] Jonathan Saul Caine, James P Evans, and Craig B Forster. Fault zone archi-
1158 tecture and permeability structure. *Geology*, 24(11):1025–1028, 1996.
- 1159 [18] Thibault Candela and Emily E Brodsky. The minimum scale of grooving on
1160 faults. *Geology*, 44(8):603–606, 2016.

- 1161 [19] Thibault Candela, François Renard, Michel Bouchon, Alexandre Brouste,
1162 David Marsan, Jean Schmittbuhl, and Christophe Voisin. Characterization
1163 of fault roughness at various scales: Implications of three-dimensional high
1164 resolution topography measurements. *Mechanics, Structure and Evolution of*
1165 *Fault Zones*, pages 1817–1851, 2010.
- 1166 [20] Thibault Candela, François Renard, Michel Bouchon, Jean Schmittbuhl, and
1167 Emily E Brodsky. Stress drop during earthquakes: effect of fault roughness
1168 scaling. *Bulletin of the Seismological Society of America*, 101(5):2369–2387,
1169 2011.
- 1170 [21] Thibault Candela, François Renard, Yann Klinger, Karen Mair, Jean Schmit-
1171 tbuhl, and Emily E Brodsky. Roughness of fault surfaces over nine decades of
1172 length scales. *Journal of Geophysical Research: Solid Earth*, 117(B8), 2012.
- 1173 [22] Thibault Candela, François Renard, Jean Schmittbuhl, Michel Bouchon, and
1174 Emily E Brodsky. Fault slip distribution and fault roughness. *Geophysical*
1175 *Journal International*, 187(2):959–968, 2011.
- 1176 [23] G Chambon, J Schmittbuhl, A Corfdir, N Orellana, M Diraison, and
1177 Y Géraud. The thickness of faults: From laboratory experiments to field
1178 scale observations. *Tectonophysics*, 426(1):77–94, 2006.
- 1179 [24] FM Chester and JM Logan. Implications for mechanical properties of brittle
1180 faults from observations of the punchbowl fault zone, California. *Pure and*
1181 *Applied Geophysics*, 124(1-2):79–106, 1986.

- 1182 [25] FM Chester and JM Logan. Composite planar fabric of gouge from the punch-
1183 bowl fault, California. *Journal of Structural Geology*, 9(5-6):621IN5–634IN6,
1184 1987.
- 1185 [26] Frederick M Chester and Judith S Chester. Stress and deformation along
1186 wavy frictional faults. *Journal of Geophysical Research: Solid Earth*,
1187 105(B10):23421–23430, 2000.
- 1188 [27] Judith S Chester and Raymond C Fletcher. Stress distribution and failure in
1189 anisotropic rock near a bend on a weak fault. *Journal of Geophysical Research:*
1190 *Solid Earth*, 102(B1):693–708, 1997.
- 1191 [28] Michele L Cooke. Fracture localization along faults with spatially varying fric-
1192 tion. *Journal of Geophysical Research: Solid Earth*, 102(B10):22425–22434,
1193 1997.
- 1194 [29] ML Cooke and DD Pollard. Bedding-plane slip in initial stages of fault-related
1195 folding. *Journal of Structural Geology*, 19(3-4):567–581, 1997.
- 1196 [30] Steven L Crouch and AM Starfield. *Boundary element methods in solid me-*
1197 *chanics: with applications in rock mechanics and geological engineering*. Allen
1198 & Unwin, 1982.
- 1199 [31] Nicholas C Davatzes, Atilla Aydin, and Peter Eichhubl. Overprinting fault-
1200 ing mechanisms during the development of multiple fault sets in sandstone,
1201 chimney rock fault array, Utah, USA. *Tectonophysics*, 363(1):1–18, 2003.

- 1202 [32] Guy Davidesko, Amir Sagy, and Yossef H Hatzor. Evolution of slip sur-
1203 face roughness through shear. *Geophysical Research Letters*, 41(5):1492–1498,
1204 2014.
- 1205 [33] James H Dieterich and Deborah Elaine Smith. Nonplanar faults: Mechanics
1206 of slip and off-fault damage. In *Mechanics, Structure and Evolution of Fault*
1207 *Zones*, pages 1799–1815. Springer, 2009.
- 1208 [34] Eric M Dunham, David Belanger, Lin Cong, and Jeremy E Kozdon. Earth-
1209 quake ruptures with strongly rate-weakening friction and off-fault plasticity,
1210 part 2: Nonplanar faults. *Bulletin of the Seismological Society of America*,
1211 101(5):2308–2322, 2011.
- 1212 [35] James T Engelder. Cataclasis and the generation of fault gouge. *Geological*
1213 *Society of America Bulletin*, 85(10):1515–1522, 1974.
- 1214 [36] Zijun Fang and Eric M Dunham. Additional shear resistance from fault rough-
1215 ness and stress levels on geometrically complex faults. *Journal of Geophysical*
1216 *Research: Solid Earth*, 118(7):3642–3654, 2013.
- 1217 [37] Haakon Fossen, Richard A Schultz, Zoe K Shipton, and Karen Mair. De-
1218 formation bands in sandstone: a review. *Journal of the Geological Society*,
1219 164(4):755–769, 2007.
- 1220 [38] JA Greenwood and JBP Williamson. Contact of nominally flat surfaces. In
1221 *Proceedings of the Royal Society of London A: Mathematical, Physical and*
1222 *Engineering Sciences*, volume 295, pages 300–319. The Royal Society, 1966.

- 1223 [39] W Ashley Griffith, Stefan Nielsen, Giulio Di Toro, and Steven AF Smith.
1224 Rough faults, distributed weakening, and off-fault deformation. *Journal of*
1225 *Geophysical Research: Solid Earth*, 115(B8), 2010.
- 1226 [40] Christopher Harbord, Stefan Nielsen, and Nicola De Paola. Fault zone rough-
1227 ness controls slip stability. In *EGU General Assembly Conference Abstracts*,
1228 volume 18, page 9799, 2016.
- 1229 [41] Rebecca M Harrington and Emily Brodsky. Smooth, mature faults radiate
1230 more energy than rough, immature faults in parkfield, ca. *Bulletin of the*
1231 *Seismological Society of America*, 99(4):2323–2334, 2009.
- 1232 [42] RR Jones, S Kokkalas, and KJW McCaffrey. Quantitative analysis and visual-
1233 ization of nonplanar fault surfaces using terrestrial laser scanning (lidar)—the
1234 arkitsa fault, central greece, as a case study. *Geosphere*, 5(6):465–482, 2009.
- 1235 [43] Bill Kilsdonk and Raymond C Fletcher. An analytical model of hanging-wall
1236 and footwall deformation at ramps on normal and thrust faults. *Tectono-*
1237 *physics*, 163(1-2):153–168, 1989.
- 1238 [44] S Kokkalas, RR Jones, KJW McCaffrey, and P Clegg. Quantitative fault anal-
1239 ysis at arkitsa, central greece, using terrestrial laser-scanning (lidar). *Bulletin*
1240 *of the Geological Society of Greece*, 37:1–14, 2007.
- 1241 [45] RW Krantz. Orthorhombic fault patterns and three-dimensional strain analy-
1242 sis, northern san rafael swell, utah. In *Geological Society of America Abstracts*
1243 *with Programs*, volume 18, page 125, 1986.

- 1244 [46] Thorne Lay, Hiroo Kanamori, and Larry Ruff. *The asperity model and the*
1245 *nature of large subduction zone earthquakes.* na, 1982.
- 1246 [47] Joong-Jeek Lee and Ronald L Bruhn. Structural anisotropy of normal fault
1247 surfaces. *Journal of Structural Geology*, 18(8):1043–1059, 1996.
- 1248 [48] Alan V Levy and Nancy Jee. Unlubricated sliding wear of ceramic materials.
1249 *Wear*, 121(3):363–380, 1988.
- 1250 [49] Laurent Maerten, David D Pollard, and Frantz Maerten. Digital mapping of
1251 three-dimensional structures of the chimney rock fault system, central utah.
1252 *Journal of Structural Geology*, 23(4):585–592, 2001.
- 1253 [50] Benoit B Mandelbrot. Self-affine fractals and fractal dimension. *Physica*
1254 *scripta*, 32(4):257, 1985.
- 1255 [51] Benoit B Mandelbrot, Dann E Passoja, and Alvin J Paullay. Fractal character
1256 of fracture surfaces of metals. 1984.
- 1257 [52] Jessica A McBeck, Elizabeth H Madden, and Michele L Cooke. Growth by
1258 optimization of work (grow): A new modeling tool that predicts fault growth
1259 through work minimization. *Computers & Geosciences*, 88:142–151, 2016.
- 1260 [53] KR McClay and PG Ellis. Analogue models of extensional fault geometries.
1261 *Geological Society, London, Special Publications*, 28(1):109–125, 1987.
- 1262 [54] HC Meng and KC Ludema. Wear models and predictive equations: their form
1263 and content. *Wear*, 181:443–457, 1995.

- 1264 [55] MS Moreno, J Bolte, J Klotz, and Dr Melnick. Impact of megathrust geometry
1265 on inversion of coseismic slip from geodetic data: Application to the 1960 chile
1266 earthquake. *Geophysical Research Letters*, 36(16), 2009.
- 1267 [56] Yoshimitsu Okada. Internal deformation due to shear and tensile faults in a
1268 half-space. *Bulletin of the Seismological Society of America*, 82(2):1018–1040,
1269 1992.
- 1270 [57] Paul G Okubo and James H Dieterich. Effects of physical fault properties on
1271 frictional instabilities produced on simulated faults. *Journal of Geophysical
1272 Research: Solid Earth*, 89(B7):5817–5827, 1984.
- 1273 [58] Andrew Clennel Palmer and JR Rice. The growth of slip surfaces in the pro-
1274 gressive failure of over-consolidated clay. In *Proceedings of the Royal Society
1275 of London A: Mathematical, Physical and Engineering Sciences*, volume 332,
1276 pages 527–548. The Royal Society, 1973.
- 1277 [59] William L Power and Terry E Tullis. Euclidean and fractal models for the
1278 description of rock surface roughness. *Journal of Geophysical Research: Solid
1279 Earth*, 96(B1):415–424, 1991.
- 1280 [60] William L Power, Terry E Tullis, and John D Weeks. Roughness and
1281 wear during brittle faulting. *Journal of Geophysical Research: Solid Earth*,
1282 93(B12):15268–15278, 1988.
- 1283 [61] WL Power, TE Tullis, SR Brown, GN Boitnott, and CH Scholz. Roughness
1284 of natural fault surfaces. *Geophysical Research Letters*, 14(1):29–32, 1987.

- 1285 [62] CA Queener, TC Smith, and WL Mitchell. Transient wear of machine parts.
1286 *Wear*, 8(5):391–400, 1965.
- 1287 [63] Elizabeth Ritz, David D Pollard, and Michael Ferris. The influence of fault
1288 geometry on small strike-slip fault mechanics. *Journal of Structural Geology*,
1289 73:49–63, 2015.
- 1290 [64] Eugene C Robertson et al. Continuous formation of gouge and breccia during
1291 fault displacement. In *The 23rd US Symposium on Rock Mechanics (USRMS)*.
1292 American Rock Mechanics Association, 1982.
- 1293 [65] Amir Sagy and Emily E Brodsky. Geometric and rheological asperities in an
1294 exposed fault zone. *Journal of Geophysical Research: Solid Earth*, 114(B2),
1295 2009.
- 1296 [66] Amir Sagy, Emily E Brodsky, and Gary J Axen. Evolution of fault-surface
1297 roughness with slip. *Geology*, 35(3):283–286, 2007.
- 1298 [67] Francois Saucier, Eugene Humphreys, and Ray Weldon. Stress near geo-
1299 metrically complex strike-slip faults: application to the san andreas fault at
1300 cajon pass, southern california. *Journal of Geophysical Research: Solid Earth*,
1301 97(B4):5081–5094, 1992.
- 1302 [68] Heather M Savage and Michele L Cooke. Unlocking the effects of friction on
1303 fault damage zones. *Journal of Structural Geology*, 32(11):1732–1741, 2010.
- 1304 [69] Jean Schmittbuhl, Sylvie Gentier, and Stéphane Roux. Field measurements of
1305 the roughness of fault surfaces. *Geophysical Research Letters*, 20(8):639–641,
1306 1993.

- 1307 [70] Jean Schmittbuhl, Francois Schmitt, and Christopher Scholz. Scaling in-
1308 variance of crack surfaces. *Journal of Geophysical Research: Solid Earth*,
1309 100(B4):5953–5973, 1995.
- 1310 [71] Jean Schmittbuhl, Jean-Pierre Vilotte, and Stéphane Roux. Reliability of
1311 self-affine measurements. *Physical Review E*, 51(1):131, 1995.
- 1312 [72] CH Scholz and JT Engelder. The role of asperity indentation and ploughing
1313 in rock friction—i: Asperity creep and stick-slip. In *International Journal of*
1314 *Rock Mechanics and Mining Sciences & Geomechanics Abstracts*, volume 13,
1315 pages 149–154. Elsevier, 1976.
- 1316 [73] Ch H Scholz and CA Aviles. The fractal geometry of faults and faulting.
1317 *Earthquake source mechanics*, pages 147–155, 1986.
- 1318 [74] Christopher H Scholz. Wear and gouge formation in brittle faulting. *Geology*,
1319 15(6):493–495, 1987.
- 1320 [75] Paul Segall and DD Pollard. Mechanics of discontinuous faults. *Journal of*
1321 *Geophysical Research: Solid Earth*, 85(B8):4337–4350, 1980.
- 1322 [76] Katherine AH Shervais and James D Kirkpatrick. Smoothing and re-
1323 roughening processes: The geometric evolution of a single fault zone. *Journal*
1324 *of Structural Geology*, 91:130–143, 2016.
- 1325 [77] Zheqiang Shi and Steven M Day. Rupture dynamics and ground motion from
1326 3-d rough-fault simulations. *Journal of Geophysical Research: Solid Earth*,
1327 118(3):1122–1141, 2013.

- 1328 [78] Zoe K Shipton, Aisling M Soden, James D Kirkpatrick, Aileen M Bright, and
1329 Rebecca J Lunn. How thick is a fault? fault displacement-thickness scaling
1330 revisited. *Earthquakes: Radiated energy and the physics of faulting*, pages
1331 193–198, 2006.
- 1332 [79] RH Sibson. Fault rocks and fault mechanisms. *Journal of the Geological
1333 Society*, 133(3):191–213, 1977.
- 1334 [80] Richard H Sibson. Crustal stress, faulting and fluid flow. *Geological Society,
1335 London, Special Publications*, 78(1):69–84, 1994.
- 1336 [81] Mark W Stirling, Steven G Wesnousky, and Kunihiko Shimazaki. Fault trace
1337 complexity, cumulative slip, and the shape of the magnitude-frequency dis-
1338 tribution for strike-slip faults: a global survey. *Geophysical Journal Interna-
1339 tional*, 124(3):833–868, 1996.
- 1340 [82] R Summers and J Byerlee. A note on the effect of fault gouge composition on
1341 the stability of frictional sliding. In *International Journal of Rock Mechanics
1342 and Mining Sciences & Geomechanics Abstracts*, volume 14, pages 155–160.
1343 Elsevier, 1977.
- 1344 [83] Mark T Swanson. Sidewall ripouts in strike-slip faults. *Journal of Structural
1345 Geology*, 11(8):933–948, 1989.
- 1346 [84] Weibin Wang and Christopher H Scholz. Wear processes during frictional
1347 sliding of rock: a theoretical and experimental study. *JOURNAL OF GEO-
1348 PHYSICAL RESEARCH-ALL SERIES-*, 99:6789–6789, 1994.

- 1349 [85] Naoto YOSHIOKA. Fracture energy and the variation of gouge and surface
1350 roughness during frictional sliding of rocks. *Journal of Physics of the Earth*,
1351 34(4):335–355, 1986.
- 1352 [86] O Zielke, M Galis, and PM Mai. Fault roughness and strength heterogene-
1353 ity control earthquake size and stress drop. *Geophysical Research Letters*,
1354 44(2):777–783, 2017.
- 1355 [87] Olaf Zielke and Paul Martin Mai. Sub-patch roughness in earthquake rupture
1356 investigations. *Geophysical Research Letters*, 2016.

1357 8 Appendix

1358 8.1 Surface Processing scripts

1359 Or possibly a link to a git repository...

1360 8.2 User manual for script

1361 This manual should serve as both a basic guide to the logic and usage of the *surface*
1362 *processing package*.

1363 The master function of the package is *surfaceprocessing*. This function effec-
1364 tively deal with the inputs and direct computations towards the necessary func-
1365 tions. Outputs of the function are a .mat workspace file for each input data file.
1366 The workspace includes a structure (called *parameters*) with the raw surface anal-
1367 ysis outputs, the point spacing, the decimation factor (if any), the file name and
1368 the date of the analysis. The workspace also includes the grid form of the origi-

nal inputed surface (called *surface*), and the pre-processed copy that was used for the subsequent analysis (called *zGrid*). Inputs are always included in pairs. The former defines the type of input, the latter qualifies or quantifies the input. This structure allows for adaptability of the code to various needs. Options include the following:

• *what to do?*: 'toDo', followed by the desired analyses on of: 'FFT', 'PLOMB', 'parameters' or 'all' (default is 'all') - can be a cell array. This specifies what kind of spatial analysis will be done on the input surface data. The spatial analysis is calculated and averaged across every single profiles along the surface. The analyses are the following:

- 'FFT', a power spectrum computed using a Fast Fourier Transform (FFT) algorithm;
- 'PLOMB', a power spectrum computed using a least-squares Lomb-Scargle algorithm;
- 'paramters', the calculation (as a function of scale) of the Root Mean Squared (RMS), skewness, kurtosis and asymmetry averaged across all segments of a given length on all profiles of the surface.

'all' simply performs all the analyses outlined above.

• *skip pre-processing?*: 'bypass', followed by 'zygo', 'pre-processing' or 'no' to be used input is already in aligned clean grid form - input files are then (default is 'no'). 'zygo' is specifically adapted to the proprietary data format of the white light in Wong. 'pre-processing' simply skips any pre-processing. This option requires a .mat structure with a field named 'grid' with the

1392 topography and a field name 'pointSpacing' specifying the point spacing (in
1393 meters). In either case the topography must be aligned such that the positive
1394 x direction is the parallel direction.

1395 • *for the parameter analysis, how many scales?* 'numberOfScales' followed
1396 by the desired number of analysed scales. This option is relevant to the
1397 parameters analysis. Note that this has a lot of effect on the amount of
1398 processing time (default is 10).

1399 • *decimation:* 'decimationFactor' followed by the desired decimation factor
1400 (default is 1). Decimation is a useful tool to reduce computation time. The
1401 surface grid is sub-sampled according to the decimation such that a decima-
1402 tion factor of k would imply that only every k th point on the every k th will
1403 be considered for hte subsequent analysis.

1404 • *Instrument specific analysis* 'instrument' followed by 'white light', 'laser
1405 scanner' or 'lidar' (default does not set any instrument specific adjustments).
1406 Some instrument specific pre-processing steps are taken. Please contact me
1407 if you intend to use this as they may be highly dependent on the specific
1408 instrument used.

1409 For instance, `surfaceprocessing('todo','FFT','bypass','zygo')` will only perform
1410 a power spectral density analysis and will skip preprocessing and assume that all
1411 input will be in the 'zygo' export .xyz format.

1412 When the command is executed, the user will be prompted to navigate to the
1413 directory where the input data is located. IMPORTANT: the directory must *only*
1414 contain files of one data format. There cannot be other files or sub-directories

1415 in the directory. The user will then be prompted to choose a destination for the
1416 output data. The requirements for the output location are less stringent. However,
1417 it is advisable to choose an empty directory such as to facilitate subsequent steps.

1418 The next step is to visualize the output of the analysis. This is done using the
1419 *unpack parameters* function. This function provides various visualization options
1420 for all files in the directory chosen by the user. The first input (the *desired plot*)
1421 can be one of the following:

1422 '*FFT*': plot all power spectra;

1423 '*PLOMB*': periodogram plot as determined by the Lomb-Scargle least squares
1424 analysis;

1425 '*topostd*': plot of the root mean squared (RMS) as a function of scale;

1426 '*topoSkew*': plot of skewness of height fields as a function of segment scale;

1427 '*topoKurt*': plot of the the kurtoisis of height fields as a function of segment
1428 scale;

1429 '*PowerVsDisp*': plot of power interpolated at a given scale as a function of
1430 displacement;

1431 '*RMSVsDisp*': model RMS at a given scale as a function of displacement

1432 '*Grids*': shows both the original and pre-processed grid for the specified file
1433 '*fileName*';

1434 '*Best Fits*': best logarithmic fits to power spectra obtained from the fast
1435 fourrier transform analysis.

1436 The functionality of the packages is broadly divided into three sections: 1)
1437 importing and preprocessing data, 2) performing various spatial statistics on the
1438 pre-processed data, and 3) unpacking the analysis output into figures.

1439 In order to run smoothly the all functions included in the package should be
1440 kept in the same directory or on an accessible path.

1441 For reference, here is a quick outline of what each function does:

1442 *affine.fit*: (from mathworks) Computes the plane of best fit using least
1443 squares normal distance;

1444 *align.grid*: finds the smoothest directions in a grid using FFT spectra and
1445 rotates and re-grids the input grid;

1446 *fault.spectral.density.simple*: Calculates the average lomb-scargle spectral
1447 density every row of a N by M array;

1448 *FindErr.loop.anisotropy*

1449 *flatten.XYZ*: removes planar trends from XYZ data by applying a rotations
1450 matrix according to the best fit plane (*affine.fit*);

1451 *fractal.model.outlier*: Removes outlying segments according to a near-gaussian
1452 model for the distribution of RMS values at specified segment lengths (or
1453 scales);

1454 *frequency.spectrum*: Calculates the average lomb-scargle spectral density of
1455 all continuous segments on every single row of a N by M array;

1456 *parse.zygo.format*: extracts the both the point spacing and topographic grid
1457 from the exported zygo format. Can also remove planar trend from data

1458 (substracted from grid);

1459 *rotateZ*: applies rotation matrix on XYZ data

1460 *surface analysis*: Aggregates the analysis functions and applies them to an

1461 input grid

1462 *surface cleaning*: removes outliers associated to surface defects

1463 *surface parameters*: calculates spatial statistics and parameters along seg-

1464 ments as a function of scale (RMS, skewness, directional asymmetry and

1465 kurtosis)

1466 *surface preprocessing 2*: deals with preprocessing input data (import data,

1467 cleaning and gridding data)

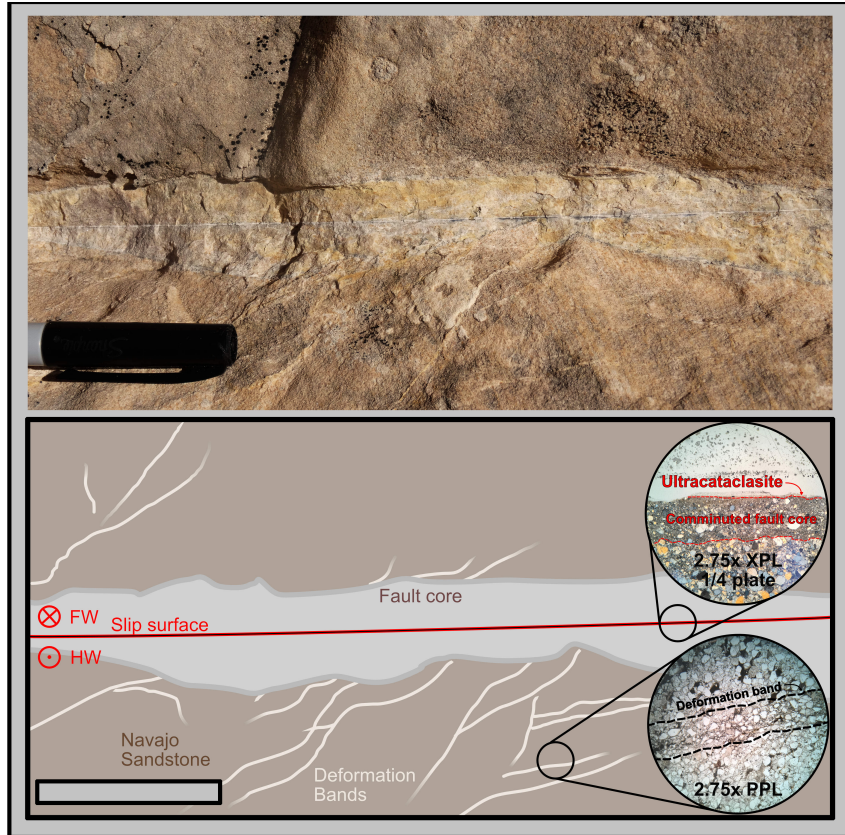


Figure 4: Top: Example of representative meso-structure of faults in the Navajo sandstone. Bottom: Cartoon of the representative meso-structure with slip surface (red), fault core (grey), deformation bands (pale beige) and intact host sand stone (brown). Upper half is the footwall; lower half is the hanging wall. Exposure is slip perpendicular. Representative thin sections show (not in situ) show the bottom half of the fault core (top) and deformation band (bottom). The section through the slip surface shows the microstructural architecture of slip surfaces with a very fine layer (barely visible) of ultra-cataclasite and a bounding comminuted layer. Note that this section is still well within the fault core. The section through the deformation bands shows the gradational reduction in grain size (outlined by black dashed line).



Figure 5: Left: Example of at least two distinct polished slip surfaces on the same fault structure. Right: Example of concentric pattern on cross-sectional view a fault

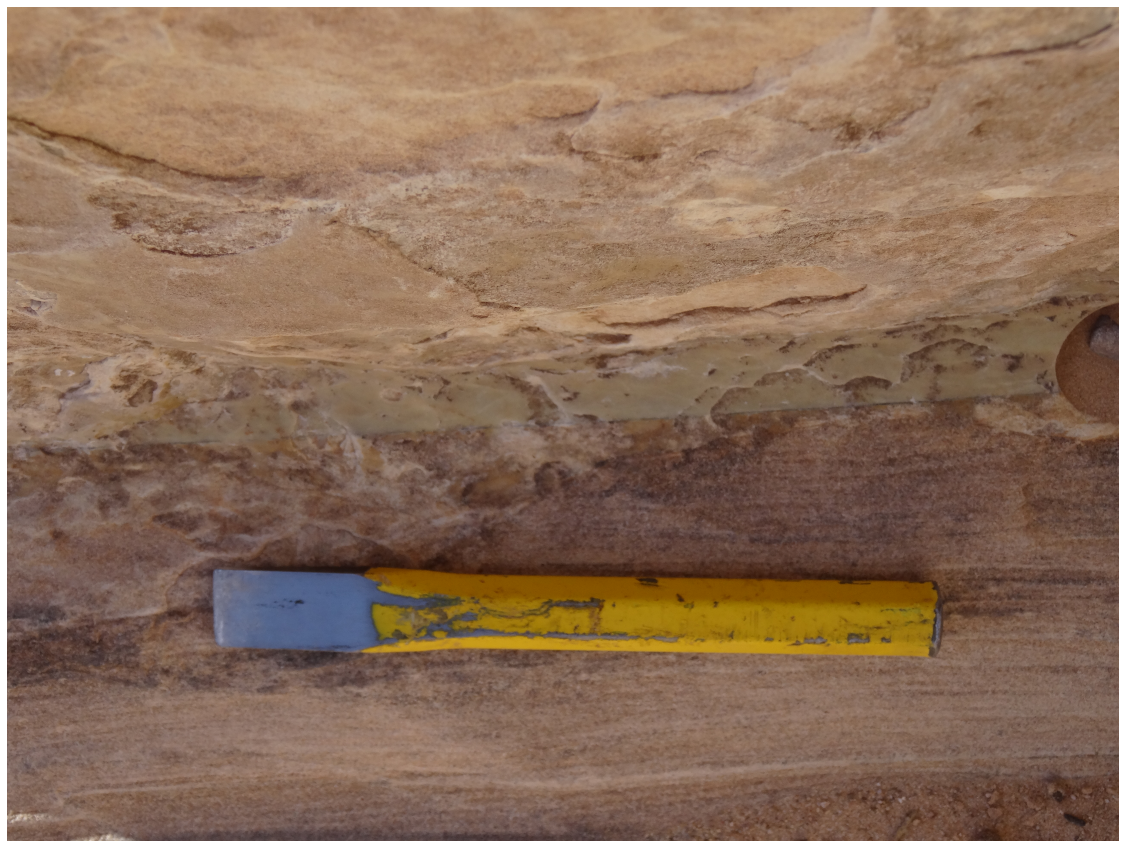


Figure 6: Example of a slip surface interpreted as a principle slip surface with around 20 meters of displacement at Big Hole Fault